All-Sky Modelling of Galactic Emission at Radio–Microwave Frequencies

Gabriel. A. Hoerning,[1]★ Stuart. E. Harper,[1] Clive Dickinson,[1] J. Patrick Leahy,[1] Roke Cepeda-Arroita,[2,3] Vasundhara Shaw,[1,4] Angela C. Taylor,[5] Michael E. Jones,[5] Jammie Leech,[5] Gilles Weymann-Despres,[5] Timothy J. Pearson,[6] and Michael W. Peel [7]

[1]*Jodrell Bank Centre for Astrophysics, Department of Physics & Astronomy, The University of Manchester, Oxford Road, Manchester, M13 9PL, U.K.*
[2]*Instituto de Astrofísica de Canarias, 38200 La Laguna, Tenerife, Canary Islands, Spain*
[3]*Departamento de Astrofísica, Universidad de La Laguna (ULL), 38206 La Laguna, Tenerife, Spain*
[4]*FIZ Karlsruhe – Leibniz-Institute for Information Infrastructure, Franklinstr. 11, 10587 Berlin, Germany*
[5]*Department of Physics, University of Oxford, Denys Wilkinson Building, Keble Road, Oxford, OX1 3RH, UK*
[6]*Cahill Centre for Astronomy and Astrophysics, California Institute of Technology, Pasadena, CA 91125, USA*
[7]*Imperial College London, Blackett Lab, Prince Consort Road, London SW7 2AZ, UK*

Accepted XXX. Received YYY; in original form ZZZ

ABSTRACT

We present a new all-sky model of low-frequency diffuse Galactic emission describing the regime where synchrotron, free–free, and spinning dust emission dominate. The model extends the *Planck* 2015 diffuse component-separation by incorporating modern radio and microwave surveys. We fit 35 full- and partial-sky maps, at 1° resolution, including S-PASS (2.30 GHz), C-BASS (4.76 GHz), and QUIJOTE (11–19 GHz), together with reprocessed WMAP and *Planck* LFI data from the Cosmoglobe collaboration and *Planck* HFI channels. Using a Bayesian parametric approach with `Commander`, we derive spatially varying amplitude and spectral parameter maps for the dominant low-frequency foreground components in total intensity. The main products of this work are: (i) a new full-sky synchrotron amplitude and spectral index solution, (ii) an all-sky characterisation of spinning dust emission based on a single-component log-normal spectral model, including peak frequency and width, and (iii) a new all-sky reconstruction at 4.76 GHz providing a tracer of diffuse synchrotron emission with reduced systematics relative to the Haslam map. The resulting model achieves RMS temperature residuals below 10 µK over 95% of the sky for frequencies up to 353 GHz, with fractional residuals below 1.5% in the Galactic plane and below 5% across QUIJOTE bands. Residual angular power spectra lie more than two orders of magnitude below the CMB spectrum, indicating noise-dominated fits on the angular scales considered. These products describe the transition between radio and microwave emission and provide a new reference for foreground modelling and sky-simulation applications.

Key words: ISM: general – cosmology: observation – cosmic microwave background – diffuse radiation – Galaxy: general

1 INTRODUCTION

Large-scale observations of the radio and microwave sky contain several astrophysical signals originating from both Galactic and extragalactic sources together with the cosmic microwave background (CMB). At low frequencies ($\lesssim 10$ GHz), synchrotron emission from the propagation of cosmic rays through the Galactic magnetic field dominates the sky (Strong et al. 2011). Around 10–30 GHz, thermal free–free emission from ionised gas (Dickinson et al. 2003), and spinning dust emission from the rapid rotation of small grains in the interstellar medium (ISM) (Dickinson et al. 2018) become prominent. At higher frequencies ($\gtrsim 100$ GHz), thermal dust emission from grains in equilibrium with the interstellar radiation field becomes the dominant diffuse Galactic component (Planck Collaboration XI 2014). Accurate modelling and separation of these components is crucial for a wide range of astrophysical and cosmological analyses, including characterisation of the ISM through cosmic-ray propagation (e.g. Strong et al. 2011), magnetic turbulence (e.g. Brandenburg & Lazarian 2013), dust grain physics (e.g. Draine 2011), the study of Galactic magnetic fields (e.g. Han 2017), and the extraction of the CMB (e.g. Remazeilles et al. 2016). However, this task remains challenging because, except for free–free emission, the spectral energy distributions (SEDs) of the dominant components are not well constrained a priori, and their relative contributions become comparable in the radio-to-microwave transition region. As a result, degeneracies between synchrotron, free–free, and spinning dust emission remain significant, especially on large angular scales and in the Galactic plane (Bennett et al. 2003; Leach et al. 2008). These challenges are not only technical, but reflect intrinsic limitations in the available data and frequency coverage.

Several algorithms have been developed to separate these astrophysical components, each making different assumptions about the data and about the nature of the underlying signals. In the recent component separation by the *Planck* Collaboration (Planck Collaboration IV 2020), the methods that were applied were: `Commander` (Eriksen et al. 2004, 2008, Seljebotn et al. 2019), the Needlet Internal Linear

★ E-mail: gabrielamancio.hoerning@postgrad.manchester.ac.uk

Combination (NILC; Basak & Delabrouille 2012, 2013), the Spectral Matching Independent Component Analysis (SMICA; Delabrouille et al. 2003; Cardoso et al. 2008), and the Spectral Estimation Via Expectation Maximisation (SEVEM; Leach et al. 2008; Fernández-Cobos et al. 2012) that are capable of recovering the CMB with the level of accuracy required for precision cosmology, whereas approaches like Commander, SMICA, and the Generalized Needlet Internal Linear Combination (GNILC; Remazeilles et al. 2011) could also reconstruct the individual Galactic foregrounds components. As the respective products suggest, these methodologies can be split into two different approaches: "blind" methods, such as NILC and SEVEM, that do not assume explicit models for the emission mechanisms, but use statistical criteria to minimise variance and "non-blind" or parametric methods, like Commander, that use physically motivated spectral models for each component and apply Bayesian inference to fit their respective parameters. Some methods, such as SMICA and GNILC, can be called semi-blind, standing between these two cases, which utilise statistical decompositions of covariance matrices and incorporate prior knowledge. The choice between blind and non-blind algorithms is a matter of choosing between robustness to modelling assumptions and physical interpretability. For studies focusing on Galactic foregrounds, where prior knowledge of emission mechanisms is available, parametric methods such as Commander are helpful since they calculate the posteriors for each parameter. These component separation methods are also crucial for algorithms of sky modelling such as the *Planck* Sky Model (PSM; Delabrouille et al. 2013) and the Python Sky Model (PySM; Thorne et al. 2017, Zonca et al. 2021, Borrill et al. 2025), that are based on physically motivated descriptions of Galactic emission to generate realistic simulations of the radio and microwave sky. A robust separation of components, therefore, provides the foundation on which these models are constructed and tested.

Previous works that aimed to separate Galactic components in the radio and microwave regime have undergone significant evolution over the past two decades. Early analyses based only on WMAP data (Gold et al. 2009; Bennett et al. 2013) were based on template fitting using external tracers of synchrotron, free–free, and thermal dust emission, such as the 408 MHz map by Haslam et al. (1982), Hα emission (Finkbeiner 2003), and far-infrared dust templates (Finkbeiner et al. 1999) respectively. Due to limited frequency coverage (≈20–100 GHz), these studies could not independently constrain the SED of the low-frequency components. The synchrotron spectral index was typically fixed to a constant value ($\beta_s \approx -3.1$), and the spinning dust was modelled only implicitly as a dust-correlated residual. Subsequent parametric approaches, including early applications of Commander to the WMAP data (Eriksen et al. 2008), faced similar limitations, as they had to again assume spatially uniform spectral priors.

The analysis presented in Planck Collaboration X (2016), hereafter referred to as the *Planck* 2015 model, represented a significant step forward by combining *Planck*, WMAP, and Haslam total-intensity data at 1° resolution. However, in the absence of complementary low-frequency surveys closer to the CMB frequencies, such as C-BASS (Jones et al. 2018, Taylor et al. in prep.), S-PASS (Carretti et al. 2019), and QUIJOTE (Rubiño-Martín et al. 2023), simplified assumptions were still necessary. Two examples are a spatially constant synchrotron spectral index and a phenomenological two-component spinning dust model with fixed SED width. In its latest release, the *Planck* Collaboration (Planck Collaboration IV 2020) adopted a fully self-consistent component separation using only *Planck* data, and no external inputs. They noted, however, that the resulting foreground reconstructions, aside from the CMB, were inferior to those obtained in the *Planck* 2015 model and were thus not publicly released. This outcome underscored the importance of joint analyses combining multiple datasets. More recently, the Cosmoglobe collaboration has provided updated foreground and CMB reconstructions that combine WMAP and *Planck* LFI data (Andersen et al. 2023), as well as a dedicated model of the polarised low-frequency sky (Watts et al. 2024), where both analyses show the power of the data $\lesssim 100$ GHz. With the release of the QUIJOTE maps, the QUIJOTE collaboration has also produced new component separation results in both total intensity (Fernández-Torreiro et al. 2023) and polarisation (de la Hoz et al. 2023). With the publication of these new low-frequency surveys, it is now possible to overcome several of the limitations that affected earlier analyses, enabling a more accurate and physically motivated description of the low-frequency foregrounds and providing a natural extension of the *Planck* 2015 model.

In this work, we present a new all-sky model of low-frequency diffuse Galactic emission. The model is constructed using a Bayesian parametric component-separation approach implemented with the Commander code, using the following surveys: *Planck* (Planck Collaboration II 2020, Planck Collaboration VIII 2016, Watts et al. 2023), WMAP (Bennett et al. 2013, Watts et al. 2023), C-BASS, S-PASS, and QUIJOTE. Commander is the appropriate choice for our goal, as it enables us to use physical priors and model the SED of each component This paper focuses on total intensity (Stokes *I*), with polarisation left for future work. Our analysis follows a philosophy similar to that of the *Planck* 2015 model, in which the derived parametric model serves as our benchmark for comparing our products. Each survey contributes complementary information that helps to break degeneracies among the components, improving the reconstruction. Unlike the mentioned previous studies, we do not use the Haslam 408 MHz map as a reference for synchrotron emission, which, despite its historical importance, suffers from calibration artefacts even in its improved release by Remazeilles et al. (2015). By leveraging contemporary, well-calibrated datasets, we aim to achieve a more physically motivated model of the radio and microwave sky. This approach also allows us to reassess long-standing assumptions in Galactic emission modelling, such as the use of the Haslam map as a synchrotron tracer, and to explore how modern surveys reshape our understanding of the low-frequency sky.

This paper is organised as follows. Section 2 describes the datasets used and the associated processing steps. Section 3 introduces the Commander code and the physical motivation for our parametric sky model. Section 4 presents the resulting component reconstructions and compares them with the *Planck* 2015 model. In Section 5, we assess the reliability and limitations of the model comparing with existing results in the literature. Our main conclusions are summarised in Section 6.

2 DATA SELECTION AND PROCESSING

The data set is assembled to anchor each foreground component close to the frequency range where it dominates, reducing the need for large extrapolations between widely separated radio and microwave regimes. Surveys near a few GHz constrain synchrotron emission close to CMB frequencies, intermediate-frequency data inform the transition between synchrotron, free–free, and spinning dust, and far-infrared channels anchor thermal dust. All maps are convolved to a common angular resolution of 1°. Per-pixel uncertainties are taken from the survey white-noise RMS maps, and the typical noise level of each channel at this resolution is reported in the Noise RMS column of Table 1, computed as the mean value of the corresponding RMS map after smoothing to 1°. A summary of the data sets is provided in Table 1. The analysis in this work is done in N_{SIDE} 256.

Table 1. Overview of data sets.

Instrument	Frequency [GHz]	Detector label	Resolution	Noise RMS $\sigma(1^\circ)$	Coverage used [a]	Units	Reference
S-PASS [b]	2.30		8.′9	606	$\delta < -15.^\circ6$	μK_{RJ}	Carretti et al. (2019)
C-BASS	4.76		45′	175	$\delta > -15.^\circ6$	μK_{RJ}	Taylor et al. (in prep.)
QUIJOTE [c]	11.1		55′	649	Galactic plane	μK_{CMB}	Rubiño-Martín et al. (2023)
	12.9		56′	479	(see Fig. 1)		
	16.8		39′	897			
	18.8		40′	714			
WMAP	22.8	K	53′	6.0	all-sky	μK_{CMB}	Bennett et al. (2013)
	33.0	Ka	40′	4.6			Watts et al. (2023)
	40.6	Q1	31′	5.6			
		Q2	31′	5.2			
	60.8	V1	21′	7.6			
		V2	21′	6.5			
	93.5	W1	13′	10.1			
		W2	13′	11.2			
		W3	13′	12.1			
		W4	13′	11.2			
Planck LFI	28.4	all	32.′4	2.3	all-sky	μK_{CMB}	Planck Collaboration II (2020)
	44.1	all	27.′1	2.7			Watts et al. (2023)
	70.3	all	13.′6	2.1			
Planck HFI	100	ds1	9.′7	0.9	all sky	μK_{CMB}	Planck Collaboration VIII (2016)
		ds2	9.′7	0.8			
	143	ds1	7.′2	0.7			
		ds2	7.′2	0.7			
		5	7.′2	0.9			
		6	7.′2	1.1			
		7	7.′2	1.0			
	217	1	5.′0	1.8			
		2	5.′0	1.9			
		3	5.′0	1.7			
		4	5.′0	1.8			
	353	ds2	4.′9	4.5			
		1	4.′9	3.5			
	545	2	4.′7	0.01	all-sky	MJy/sr	
		4	4.′7	0.01			
	857	2	4.′4	0.01			

Notes: [a] For S-PASS and QUIJOTE, we used a limited coverage compared to the survey's full coverage. [b] 600 µK of regularisation noise is added to the thermal noise RMS. [c] 5% calibration uncertainty is added to the thermal noise RMS.

2.1 S-PASS

The S-band Polarization All Sky Survey (S-PASS) is a southern-sky survey conducted with the Parkes telescope at 2.30 GHz (Carretti et al. 2019), with an angular resolution of 8.′9 and coverage $\delta < -1^\circ$. At this frequency, synchrotron emission dominates the diffuse sky brightness, making S-PASS a key anchor for the low-frequency synchrotron component in the southern hemisphere. The survey has an absolute calibration uncertainty of 5%. S-PASS and C-BASS overlap over roughly 16° in declination. In this region, joint use of both surveys in internal analysis lead to residual structures inconsistent with white noise, likely associated with ground pickup and scan-synchronous effects typical of ground-based large-area radio surveys. We therefore exclude S-PASS data in the overlap region and retain C-BASS there, owing to its closer frequency proximity to WMAP and *Planck* and the more extensive characterisation of its systematics. We use S-PASS only for $\delta < -15.^\circ6$. As no detailed beam model is publicly available, we adopted the native S-PASS beam as a Gaussian with FWHM 8.′9 before convolution to the common 1° resolution. The S-PASS collaboration provides RMS maps for polarisation only, so to construct an intensity uncertainty estimate, we use these RMS maps together with an additional regularisation noise of 600 µK, which yields residuals comparable to those of C-BASS in overlapping regions and avoids overweighting S-PASS in the fit.

2.2 C-BASS

The C-Band All-Sky Survey (C-BASS) provides large-area intensity maps at 4.76 GHz with an angular resolution of 45′ (Jones et al. 2018). In this work we use the northern survey (Taylor et al. in prep.), covering $\delta > -15.^\circ6$, while the southern survey is to be initiated. At

this frequency, synchrotron emission dominates over free–free and spinning dust at most latitudes, placing C-BASS at a critical transition between classical radio surveys and microwave data. It therefore serves as the primary anchor for the synchrotron component in the northern sky, replacing the traditional Haslam 408 MHz map and strongly reducing sensitivity to low-frequency spectral curvature. In combination with S-PASS in the southern hemisphere, this provides coverage of the sky at frequencies close to the CMB channels and improves the separation between synchrotron, free–free, and spinning dust emission. As a single-dish survey, C-BASS is affected by instrumental effects typical of large-area ground-based radio maps, including ground pickup and residual scan-synchronous structures. These effects are well characterised in the survey data release and are constrained to the few-per-cent level in amplitude over the relevant multipole ranges, corresponding to sub-mK fluctuations (~ 0.3–1 mK for typical I-band sky levels) on degree scales. The survey benefits from a stable instrumental design and a detailed beam model. The absolute calibration uncertainty is 5%. The native beam is convolved to the common 1° resolution used in the fit. Its frequency proximity to WMAP and *Planck* channels makes it effective in constraining the synchrotron emission parameters and in breaking degeneracies with free–free and spinning dust between 5–20 GHz (Jew et al. 2019).

2.3 QUIJOTE

The Q-U-I JOint TEnerife (QUIJOTE) experiment is a multi-frequency microwave survey conducted at the Teide Observatory, covering 10–40 GHz with angular resolutions ranging from $39'$ to $56'$ (Rubiño-Martín et al. 2012, 2023). In this work, we use total-intensity data from the Multi-Frequency Instrument (MFI) at 11.1, 12.9, 16.8, and 18.8 GHz. These frequencies probe the low-frequency side of spinning dust emission and provide direct constraints on its peak frequency and spectral width. The QUIJOTE beams are well characterised, and the native beams are convolved to the common 1° resolution. The calibration uncertainty of the MFI channels is 5%.

The MFI maps are subject to residual radio-frequency interference (RFI), which reduces the effective signal-to-noise ratio (S/N) in high-latitude regions due to lower temperature. In addition, the processing applied to mitigate RFI filters out large angular-scale modes in the maps, which can limit their use for modelling the faintest diffuse emission over wide sky areas when combined with data sets that do not undergo a similar large-scale filtering. We therefore restrict their use to regions where the sky signal is sufficiently strong to provide high S/N and good consistency with the other data sets entering the fit, which in practice favours areas closer to the Galactic plane. For the 11.1 and 12.9 GHz channels, we apply a temperature threshold of 2 µK directly on the public maps, while for the 16.8 and 18.8 GHz channels we adopt a threshold of 4 µK. The resulting masks are shown in Fig. 1. Internal `Commander` tests show that using only the thermal RMS maps for these channels leads to significant tension with the rest of the data set, indicating that additional uncertainty beyond the provided RMS is required for an internally consistent multi-survey fit. To account for this, we increase the per-pixel uncertainty by adding in quadrature a term corresponding to 5% of the local map intensity, effectively down-weighting QUIJOTE and treating the calibration uncertainty as spatially uncorrelated. Given that the QUIJOTE data are restricted in this work to bright Galactic-plane regions, where small angular scales dominate the signal, and that the additional uncertainty term increases the flexibility of the fit, the impact of the large-scale filtering on the recovered spectral parameters is expected to be subdominant. Despite this conservative treatment, the QUIJOTE channels retain sufficient constraining power to improve the determination of the synchrotron, free–free, and spinning dust spectral parameters.

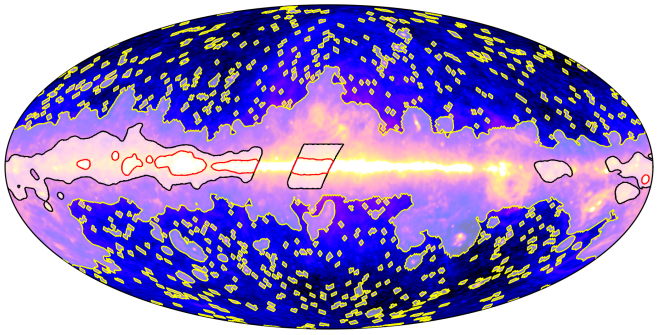

Figure 1. WMAP K-band (22.8 GHz) map with the CMB signal subtracted, overlaid with the masks used for free–free emission modelling and QUIJOTE data. *Black contours:* Galactic plane mask for QUIJOTE 11 and 13 GHz. *Red contours:* Galactic plane mask for QUIJOTE 17 and 19 GHz. *Yellow contours:* FF47 mask. Opaque regions are where pixel fitting for free–free emission is performed, otherwise, the Hα map is adopted with the respective µK/R ratio.

2.4 WMAP

We use the 9-year Wilkinson Microwave Anisotropy Probe (WMAP) temperature maps (Bennett et al. 2013), as reprocessed by the Cosmoglobe collaboration (Watts et al. 2023). WMAP provides full-sky coverage from 23 to 94 GHz, bridging the transition between radio and microwave emission and contributing to the separation of synchrotron, free–free, and spinning dust components. The Cosmoglobe reprocessing improves the treatment of large-scale systematics and calibration relative to the original WMAP releases, particularly on the largest angular scales, which are critical for constraining diffuse Galactic emission. All WMAP channels are convolved to the common 1° resolution used in this analysis, using the native beam transfer functions. The absolute calibration uncertainty is 1%. Residual beam asymmetries present in the Cosmoglobe maps introduce small-scale artefacts around bright compact sources. We mitigated using a hybrid large-scale/small-scale combination between the WMAP Cosmoglobe and DR5 maps described in Appendix A. Outside bright compact sources, these differences have negligible impact on the diffuse emission targeted in this work.

2.5 *Planck*

We use maps from the *Planck* Low Frequency Instrument (LFI) reprocessed by the Cosmoglobe collaboration (Watts et al. 2023), together with High Frequency Instrument (HFI) detector-set maps from the *Planck* 2015 release (Planck Collaboration VII 2016). The LFI channels (28.4–70.4 GHz) bridge the transition between synchrotron-dominated emission and the regime where free–free and spinning dust become important, while the HFI channels (100–857 GHz) anchor the thermal dust component. The Cosmoglobe reprocessing improves the treatment of large-scale systematics and calibration in the LFI maps, which is critical for modelling diffuse Galactic emission. We adopt the *Planck* 2015 beam profiles when smoothing the LFI maps to the common 1° resolution, as use of the 2018 beams was found to introduce non-astrophysical artefacts in residual maps aligned with the HEALPix projection near the Galactic poles. The HFI 2015 detector-set maps provide access to single-bolometer data, facilitating the separation of CO and HCN line emission in the sky model (Section 3.2), and are the same data sets used in the *Planck* 2015 model.

The calibration uncertainty is 1% for all *Planck* channels, except for 353 GHz (1.3%), 545 GHz (6.0%), and 857 GHz (6.4%).

3 SKY MODEL AND INFERENCE

In this section, we define the parametric sky model adopted in `Commander`, including the diffuse components, their SEDs, and the physical motivation for each term. The main modifications relative to previous implementations concern the low-frequency foregrounds, while the treatment of molecular line emission, thermal dust, and instrumental parameters follows the approach adopted in the *Planck* 2015 model.

3.1 COMMANDER

We perform the component separation using the Bayesian parametric framework `Commander` (Eriksen et al. 2004; Eriksen et al. 2008; Planck Collaboration X 2016), which fits an explicit physical model of the sky to multi-frequency observations in pixel space. For each frequency channel ν, the data are modelled as

$$\mathbf{d}_\nu = \sum_i F_\nu^i(\boldsymbol{\beta}_i, \Delta_\nu)\, \mathbf{a}_i + T_\nu\, \mathbf{m}_\nu + \mathbf{n}_\nu, \tag{1}$$

where $\mathbf{a}_i$ are component amplitude maps at reference frequencies, $\boldsymbol{\beta}_i$ are spectral parameters, F_ν^i encodes the frequency dependence including bandpass and unit-conversion effects, Δ_ν and T_ν account for calibration and template corrections, and $\mathbf{n}_\nu$ is Gaussian noise with known covariance. All quantities are expressed in brightness temperature units. Parameter estimation proceeds by sampling the posterior distribution under Gaussian noise assumptions with informative priors that reduce degeneracies between components, including positivity constraints on amplitudes (except the CMB), Gaussian priors on spectral parameters, and fixed monopole, dipole, and calibration constraints for selected channels. We adopt the pixel-space implementation of `Commander` rather than the harmonic-space `Commander3` (Seljebotn et al. 2019; Galloway et al. 2023). Our goal is to recover spatially resolved spectral parameters and construct spectral index maps from the posterior distributions. Harmonic-space component separation mixes emission along the line-of-sight through the spherical-harmonic decomposition, effectively averaging spectral variations and limiting the recovery of local spectral information. The pixel-based approach allows direct estimation of spatially localised spectral parameters, which is essential for the scientific objectives of this work. The analysis is based on a Gibbs chain of 40 000 samples, from which the first 4 000 are discarded as burn-in and all posterior summaries presented in this work are computed from the remaining samples.

3.2 SKY MODEL

We now specify the spectral models adopted for each diffuse sky component and the physical processes they represent. The corresponding SEDs and prior values are summarised in Table 2.

CMB — The CMB SED is described by a blackbody spectrum with a single parameter, the CMB temperature $T_{\rm cmb}$. In practice, the monopole is removed from all maps and `Commander` models only the CMB anisotropies, whose frequency dependence is given by the derivative of the blackbody spectrum evaluated at $T_{\rm cmb}$. We adopt $T_{\rm cmb} = 2.7255$ K (Fixsen 2009) and fix this value in the analysis, as its uncertainty is negligible compared to other sources of error. The Cosmoglobe reprocessing includes a correction for the relativistic kinematic quadrupole that can affect low-frequency *Planck* LFI and WMAP channels (Notari & Quartin 2015). Nevertheless, we find that a small residual remains in the LFI 70 GHz map. To account for this, we include a kinematic-quadrupole template evaluated at the central frequency of this channel with a free amplitude determined through maximum-likelihood fitting. This amplitude is not sampled in the posterior analysis. The corresponding effect is negligible for the HFI channels.

Synchrotron — Diffuse synchrotron emission dominates the sky at GHz frequencies and arises from relativistic electrons spiralling in the Galactic magnetic field (Strong et al. 2011). Above a few GHz, the synchrotron spectrum is well described by a power-law with spectral index $\beta_{\rm s} \approx -3$ (Reich & Reich 1988; Kogut et al. 2007; Harper et al. 2022), while significant spectral flattening occurs at lower frequencies (de Oliveira-Costa et al. 2008; Kogut 2012). VS- I think you probably mean that C-BASS and S-PASS are high enough in frequencies that we can use a power law approximation, but when you connect this line with the previous one, it feels contradictory as you have mentioned that spectral flattening takes place at lower frequencies. Just say that C-BASS and S-PASS are high enough in frequency that we do not have to worry about spectral flattening and can use a power law profile.Since our low-frequency anchors (S-PASS at 2.30 GHz and C-BASS at 4.76 GHz) lie in the range where a simple power-law approximation is valid, we model the synchrotron SED with spatially varying amplitude $A_{\rm s}$ and spectral index $\beta_{\rm s}$. In contrast to earlier analyses, we do not include the Haslam 408 MHz map, as connecting the sub-GHz regime to GHz frequencies would require an additional curvature parameter and the map contains known large-scale systematics that can dominate fits due to its high S/N (Remazeilles et al. 2015; Wilensky et al. 2025; Nasirudin & Bull 2025). By restricting the model to frequencies above 2 GHz, we avoid the regime of strong spectral curvature and retain a physically motivated power-law description. To control degeneracies with free–free and spinning dust emission, we adopt a Gaussian prior $\beta_{\rm s} \sim \mathcal{N}(-3.1, 0.3)$, which provides sufficient flexibility while preventing unphysical solutions.

Free–free — Free–free (bremsstrahlung) emission arises from electron–ion collisions in the ionised ISM and has a well-defined spectral form governed by plasma physics (Dickinson et al. 2003; Draine 2011). We adopt the same two-parameter description as in the *Planck* 2015 model, with emission measure (EM) and electron temperature $T_{\rm e}$, but use an Hα template (Dickinson et al. 2003) as an external tracer to reduce degeneracies with synchrotron and spinning dust at high Galactic latitudes, where free–free emission is weak. The Hα-derived free–free brightness temperature is modelled with a fixed spectral index $\beta_{\rm ff} = -2.12$ and an amplitude of 195 μK R^{-1} at 4.76 GHz (equivalent to 7.04 μK R^{-1} at 22.8 GHz; Harper et al. 2022). Because Hα is strongly affected by dust extinction near the Galactic plane, we construct an extinction mask using the thermal-dust optical depth at 353 GHz (Planck Collaboration IX 2016), excluding pixels with $\tau_{353} > 10^{-5}$ (equivalent to A(H$\alpha \lesssim 0.53$)) after smoothing to 3° and combining this with the PM61 mask from the *Planck* 2015 model to define the FF47 mask, shown in Fig. 1. Outside the masked regions, the scaled Hα template is used directly, while inside the mask free–free is determined through pixel-based fitting.

Internal tests showed that freely sampling the Hα amplitude at 22.8 GHz led to its suppression in the MCMC solution, with the missing signal absorbed by synchrotron or spinning dust due to their greater spectral flexibility. To avoid this leakage, we fix

Table 2. Summary of parametric signal models.

Component	Free parameters and priors			Brightness temperature, T_b [μK_{RJ}]			Additional information
CMB	A_{cmb}	$\sim$	Uniform$(-\infty, \infty)$	x	=	$\frac{h\nu}{k_B T_{cmb}}$	$T_{cmb} = 2.7255$ K
				$g(\nu)$	=	$[\exp(x) - 1]^2/[x^2 \exp(x)]$	
				$T_{b,cmb}$	=	$A_{cmb}/g(\nu)$	
Synchrotron ...	A_s	$>$	0	$T_{b,s}$	=	$A_s \left(\frac{\nu}{\nu_{0,s}}\right)^{\beta_s}$	$\nu_{0,s} = 4.76$ GHz
	β_s	$\sim$	$N(-3.1 \pm 0.3)$				
Free–free	ln EM	$\sim$	Uniform$(-\infty, \infty)$	g_{ff}	=	$\ln\left\{\exp\left[5.960 - \sqrt{3}/\pi \log\left(\nu_9 T_4^{-3/2}\right)\right] + e\right\}$	T_e = *Planck* 2016 map
				τ	=	$0.05468\, T_e^{-3/2}\, \nu_9^{-2}\, EM\, g_{ff}$	$T_4 = T_e/10^4$
				$T_{b,ff}$	=	$10^6\, T_e (1 - e^{-\tau})$	$\nu_9 = \nu/(10^9$ Hz)
Spinning dust ...	A_{sd}	$>$	0	$T_{b,sd}$	=	$A_{sd} \exp\left\{-\frac{1}{2}\left[\frac{\ln(\nu/\nu_p)}{w}\right]^2\right\}\left(\frac{\nu_{0,sd}}{\nu}\right)^2$	$\nu_{0,sd} = 22.8$ GHz
	ν_p	$\sim$	$N(25 \pm 5$ GHz)				
	w	$\sim$	$N(0.6 \pm 0.1)$				
Thermal dust ...	A_d	$>$	0	γ	=	$\frac{h}{k_B T_d}$	$\nu_{0,d} = 545$ GHz
	β_d	$\sim$	$N(1.55 \pm 0.1)$	$T_{b,d}$	=	$A_d \left(\frac{\nu}{\nu_{0,d}}\right)^{\beta_d+1} \frac{\exp(\gamma\nu_{0,d})-1}{\exp(\gamma\nu)-1}$	
	T_d	$\sim$	$N(23 \pm 3$ K)				
SZ	y_{sz}	$>$	0	$T_{b,sz}$	=	$10^6 \frac{y_{sz} T_{cmb}}{g(\nu)} \left\{\frac{x[\exp(x)+1]}{\exp(x)-1} - 4\right\}$	
Line emission ...	A_i	$>$	0	$T_{b,i}$	=	$A_i h_{ij} \frac{F_i(\nu_j)}{F_i(\nu_{0,i})} \frac{g(\nu_{0,i})}{g(\nu_j)}$	i $\in$ {CO $J = 1 \to 0$; CO $J = 2 \to 1$; CO $J = 3 \to 2$; 94/100} j = detector index h_{ij} = *Planck* 2016 map F = unit conversion

Note: The symbol "~" implies that the respective parameter has a prior as given by the right-hand side distribution.

the Hα amplitude to 7.04 μK R^{-1} at 22.8 GHz. At high Galactic latitudes the free–free signal is only of order a few μK at this frequency, and therefore does not drive the fit. In parts of the Galactic plane, degeneracies occasionally drove the fitted free–free amplitudes below the Hα-scaled expectation. To prevent unlikely solutions, we apply a constraint similar to Gold et al. (2009), requiring $T_{b,ff}(\theta) > 0.5 \cdot 7.04\, H\alpha(\theta)$, and otherwise reverting to the scaled template. Finally, the impact of varying T_e on the recovered foreground parameters is negligible. We therefore fix T_e to the values provided by the *Planck* 2015 model.

Spinning Dust — Dust grains emit microwave radiation through rotational electric-dipole emission when they possess a permanent dipole moment. In this analysis, Anomalous Microwave Emission is modelled exclusively as spinning dust emission. Other proposed mechanisms, such as Magnetic Dipole Emission from magnetic grains (Draine & Lazarian 1999; Draine & Hensley 2013), are not included. We describe this spinning-dust component using a phenomenological log-normal SED, which provides sufficient flexibility to reproduce the observed spectra given the current frequency coverage and calibration limitations while remaining constrained by the data (Bonaldi et al. 2007; Stevenson 2014; Dickinson et al. 2018; Cepeda-Arroita et al. 2025). The model has three parameters: the amplitude A_{sd}, the peak frequency ν_p (defined in flux-density units), and the spectral width w (Table 2). Although `Commander` performs calculations in Rayleigh–Jeans (RJ) temperature units, ν_p is estimated in flux units by multiplying the SED by $(\nu_{0,sd}/\nu)^2$, since the peak frequency is not well defined in RJ units. This approach differs from the *Planck* 2015 model, which employed a two-component SED based on `SpDust2` templates (Ali-Haïmoud et al. 2009; Ali-Haïmoud 2010; Silsbee et al. 2011). Those spectral templates assume fixed spectral widths and specific interstellar environments, whereas the log-normal form allows the spectral width to vary spatially and better captures the broader spectra observed in real data (Cepeda-Arroita et al. 2025). The peak frequency depends on local grain properties and environment and is typically observed between 20–30 GHz, with higher values in some regions (Planck Collaboration Int. XV 2014; Cepeda-Arroita et al. 2025). We therefore adopt Gaussian priors $\nu_p \sim N(25\,\text{GHz}, 5\,\text{GHz})$ and $w \sim N(0.6, 0.1)$. These priors stabilise the solution in low S/N regions and help mitigate degeneracies among low-frequency foreground components without forcing the fit in well-constrained areas.

Other components — The modelling of Zodiacal emission, thermal dust, thermal Sunyaev–Zeldovich (SZ), and molecular line emission follows the strategy adopted in the *Planck* 2015 component-separation analysis. The constraints on these components arise primarily from

the *Planck* HFI 2015 frequency channels, which are also used here, and we therefore retain the same parametric forms and priors as in that work. Residual Zodiacal emission in WMAP and LFI channels is corrected through template subtraction using multiplicative factors from Table 2 of the *Planck* 2015 model, based on the 100 GHz HFI Zodiacal light template (Planck Collaboration XIV 2014).

Thermal dust emission is described by a single-component modified blackbody spectrum with three free parameters per pixel: amplitude $A_{\rm d}$, emissivity index $\beta_{\rm d}$, and dust temperature $T_{\rm d}$ (Planck Collaboration XII 2014). This model captures the large-scale Galactic dust SED over the frequency range considered (up to 857 GHz) and is consistent with the approach adopted in *Planck* 2015. More complex multi-component dust models become relevant only at higher frequencies, such as those probed by COBE–DIRBE, and are not required for the present analysis.

The thermal SZ effect arises from inverse-Compton scattering of CMB photons by hot electrons in galaxy clusters (Sunyaev & Zeldovich 1970). It is modelled using a single amplitude parameter, the Compton-y parameter $y_{\rm sz}$, with the frequency dependence fixed by the SZ spectral distortion (Table 2). Because the SZ signal is weak over most of the sky and susceptible to leakage from other components, we restrict SZ fitting to the regions around the Coma and Virgo clusters following Planck Collaboration X (2016), thereby limiting contamination of the diffuse foreground solution.

Molecular line emission from CO is modelled through separate components for the $J = 1 \rightarrow 0$ (100 GHz), $J = 2 \rightarrow 1$ (217 GHz), and $J = 3 \rightarrow 2$ (353 GHz) transitions (Planck Collaboration XIII 2014), together with an additional line near 94/100 GHz (Takekawa et al. 2014) associated with overlap between WMAP W-band and HFI 100 GHz bandpasses. Each line is described by an amplitude map A_i at the transition frequency, normalised to a reference detector. Frequency scaling is implemented through spatially constant line ratios h_{ij} and unit-conversion factors $F(\nu)$ accounting for bandpass and unit differences. Since the relevant channels and bandpasses are identical to those in the *Planck* 2015 model, the h_{ij} parameters are fixed to their 2015 values and only the amplitudes A_i are sampled.

Monopoles and dipoles — The lowest multipoles of the sky maps, corresponding to the monopole ($\ell = 0$) and dipole ($\ell = 1$) modes, are fundamentally degenerate with instrumental offsets. Differential microwave observations constrain spatial variations of the sky brightness but do not directly measure the absolute sky temperature. Physically, the sky monopole is dominated by the CMB blackbody temperature of 2.7255 K, followed at high frequencies by the mean level of the Cosmic Infrared Background (CIB) (Planck Collaboration XXX 2014), while the dominant dipole arises from the CMB kinematic dipole, measured to be 3.3655 K and 3.3640 K by LFI and HFI respectively (Planck Collaboration I 2016). However, these absolute contributions are not preserved in most microwave maps. As a consequence, only angular structure at multipoles $\ell \geq 2$ is robustly determined from the data alone, and monopole and dipole terms must be treated as offsets within the component-separation.

This limitation is reinforced by the calibration scheme of the data sets used here. WMAP and *Planck* maps are calibrated relative to the CMB dipole and processed to remove large-scale offsets, such that the mean temperature at high Galactic latitudes is close to zero by construction. As a result, these maps do not preserve the absolute sky zero level, but only relative temperature fluctuations about an arbitrary reference. Although C-BASS provides an absolute calibration tied to ARCADE 2 (Leahy et al. 2024), VS: cite Paddy's zero level paper? or if this is the zero level paper then follow the MNRAS convention and let it cite as in preparation, currently it gives the impression that the paper is already published. this cannot be adopted directly in a joint analysis unless all channels share a consistent absolute reference, which is not the case. The present work therefore operates in a relative framework, solving for monopole and dipole offsets rather than attempting to determine the true zero level of the sky. Following the strategy of the *Planck* 2015 model, we anchor a subset of channels and solve for residual monopole and dipole offsets in the remaining maps using the PM61 mask. This procedure yields a self-consistent large-scale solution for all astrophysical components while remaining insensitive to the absolute sky temperature.

The calibration of the low-frequency radio surveys is important, since residual offsets and scale differences directly affect the amplitudes and spectral indices. In this work, C-BASS sets the synchrotron amplitude scale in the northern hemisphere, while S-PASS provides the corresponding reference in the southern hemisphere through alignment in their overlap region. QUIJOTE offsets are determined within the Galactic-plane region used in the fit to ensure internal consistency of the spectral solution. Cosmoglobe-reprocessed WMAP and LFI maps retain the *Planck* 2015 model for monopole and dipole normalisation scheme with minor adjustments for the reprocessed maps. Since C-BASS and S-PASS define the reference amplitude scale for the synchrotron component in the northern and southern hemispheres, respectively, their 5% absolute calibration uncertainties propagate as multiplicative systematic uncertainties into the recovered synchrotron brightness and spectral index maps. The detailed procedures used to determine the offsets of the low-frequency surveys are described in Appendix B. A fully self-consistent determination of the absolute sky zero level lies beyond the scope of this work and will require future absolutely calibrated experiments, such as ARCADE 2 (Fixsen et al. 2011), L-BASS (Zerafa et al. 2025), and the Tenerife Microwave Spectrometer (Rubiño Martín et al. 2020).

Instrumental effects — In addition to the astrophysical parameters, the model formally includes instrumental degrees of freedom following the scheme adopted in the *Planck* 2015 model. These consist of multiplicative gain factors g_ν and effective bandpass shifts Δ_ν, which modify the mixing matrix and absorb residual inter-channel calibration and spectral-response uncertainties. Such parameters are important because calibration mismatches project directly onto the inferred spectral behaviour of the components.

In the present work, we do not sample gain parameters for C-BASS, S-PASS, or QUIJOTE. For C-BASS and S-PASS, the gain is strongly degenerate with the synchrotron amplitude, as these channels define the low-frequency anchor of that component and therefore set its overall amplitude scale. Allowing g_ν to vary would primarily redistribute power between instrumental gain and astrophysical amplitude without introducing additional constraining information. For QUIJOTE, the limited sky fraction used in the analysis leads to a similar degeneracy with local foreground amplitudes, preventing an independent determination of the gain. The gain parameters for these channels are therefore held fixed. Likewise, we do not fit bandpass-shift parameters for C-BASS, S-PASS, or QUIJOTE. Instead, the finite bandpasses of these experiments ($\approx 20\%$ for C-BASS, $\approx 7\%$ for S-PASS, and $\approx 10\%$ for QUIJOTE) are accounted for through colour corrections. These corrections are implemented using second-order polynomial expansions of the bandpass response (e.g. Peel et al. 2022), which are incorporated directly into the model prediction. For typical synchrotron spectral indices ($\beta \sim -3$), neglecting bandpass integration would bias the recovered spectral index by of order $\sim 2\%$ for C-BASS and below the percent level for S-PASS and QUIJOTE. In this way, bandpass effects are treated consistently while avoiding additional degenerate instrumental degrees of freedom. For the remaining chan-

nels, the treatment of instrumental parameters and priors follows the *Planck* 2015 model.

4 RESULTS

In this section, we present the main results obtained for the CMB and the low-frequency Galactic foregrounds. The discussion focuses on the improvements relative to the *Planck* 2015 model, which primarily arise from the revised treatment of low-frequency data and foreground components. High-frequency foregrounds ($\gtrsim 100$ GHz), including thermal dust emission and molecular line emission, are modelled following the same approach as in the previous analysis and show no significant differences and they are therefore not discussed further here. We begin by presenting the results for the CMB, synchrotron, free–free, and spinning dust emission, followed by an assessment of the goodness-of-fit. The section concludes with one of the main products of this work: a total-intensity all-sky map at 4.76 GHz. The posterior constraints on instrumental parameters, monopoles, and dipoles are summarised in Appendix B (Table B1).

4.1 CMB AND GALACTIC FOREGROUNDS

We now present the results for the CMB and the three low-frequency foreground components constrained by our analysis. Figure 2 shows the posterior mean amplitude maps together with their associated posterior standard deviations. To highlight the impact of the revised low-frequency modelling, Fig. 3 compares our posterior mean amplitudes with those obtained from the *Planck* 2015 model at a resolution of FWHM = 2°. The corresponding spectral parameters are shown in Fig. 4.

4.1.1 Cosmic Microwave Background

The CMB signal is constrained by a joint fit to WMAP and *Planck* data, with the *Planck* HFI channels providing the dominant statistical weight. As the CMB modelling and data combination are unchanged relative to the *Planck* 2015 model, no major differences in the recovered CMB component are expected. The top-left panel of Fig. 2 shows the posterior mean CMB map derived in this work. The main deviations relative to the *Planck* 2015 solution are confined to the Galactic plane, as shown in the top-left panel of Fig. 3. While differences at high Galactic latitudes remain minimal, deviations reach up to $\sim 25\%$ in the inner Galactic plane and $\sim 5\%$ in regions such as the Gum Nebula and Eridanus. These differences originate from a revised partitioning of emission among the low-frequency foregrounds, in particular synchrotron and free–free emission below ~ 20 GHz. Owing to the relatively flat free–free spectrum ($\beta_{\rm ff} \approx -2.1$), its contribution remains non-negligible up to frequencies approaching ~ 100 GHz in the Galactic plane, and residual component degeneracies can therefore indirectly affect the recovered CMB signal in these regions.

Consistent with this interpretation, the top-right panel of Fig. 2 shows an increase in the CMB posterior uncertainty in the Galactic plane relative to high latitudes. Despite these localised differences, the large-scale statistical properties of the CMB remain unchanged. Using the LM95 mask (see Section 4.2), the C_ℓ spectra agree to within 2% over the multipole range $\ell = 2$–180, indicating no significant large-scale deviation from the *Planck* 2015 model. For reference, the maximum-likelihood amplitude of the kinetic quadrupole template fitted in the LFI 70 GHz channel is 0.53 relative to its nominal normalisation.

4.1.2 Synchrotron

The synchrotron component is the foreground most affected by the modelling adopted in this work. Figure 2 shows the posterior mean synchrotron amplitude at 4.76 GHz, where the main large-scale Galactic structures and filaments, including the North Polar Spur and the principal radio loops, are clearly recovered. The spatial morphology is consistent with previous analyses, indicating that the dominant difference relative to the *Planck* 2015 model lies in the overall normalisation rather than in the morphology of the emission. This is quantified through a T–T analysis between our synchrotron map and the *Planck* 2015 synchrotron prediction evaluated at 4.76 GHz, performed at $N_{\rm SIDE} = 64$, masking unreliable regions with the LM95 mask (see Section 4.2) and excluding compact sources using the LFI 30 GHz point-source mask (PS30). The resulting Spearman rank coefficient of $r_{\rm s} = 0.94$ confirms the strong morphological agreement, while the best-fitting slope of 0.47 ± 0.02 indicates that the *Planck* 2015 model underestimates the synchrotron amplitude at 4.76 GHz by approximately 50%. This offset arises from the revised low-frequency modelling adopted here, which anchors the synchrotron component directly at 2.30 and 4.76 GHz rather than extrapolating from 408 MHz. A T–T analysis between C-BASS and the Haslam 408 MHz map yields a spectral index of $\beta_{0.408-4.76} = -2.82 \pm 0.02$, flatter than the $\beta \approx -3.1$ assumed over the same frequency range in the *Planck* 2015 model. The resulting spectral difference of $\Delta\beta_{\rm s} = -0.26 \pm 0.02$ implies an amplitude shift of approximately 50% between 0.408 and 4.76 GHz, fully accounting for the normalisation offset observed in the T–T comparison.

Beyond this modelling difference, the fractional-difference maps shown in Fig. 3 provide evidence that the earlier solution was affected by large-scale systematics. Two independent signatures support this interpretation: (i) residual structures aligned with the Haslam scan strategy, which are identifiable by eye in the original unreprocessed 408 MHz map, and (ii) sharp morphological boundaries that spatially coincide with the transitions between the individual surveys composing the Haslam atlas. These features are absent in our solution, indicating that the revised synchrotron map is largely free of such artefacts. The higher synchrotron normalisation recovered here therefore reflects both the improved low-frequency modelling and the mitigation of Haslam-related systematics. In the 20–40 GHz range, the corresponding amplitude differences are typically 3–15 μK.

The synchrotron spectral index map provides an additional and independent validation of the revised low-frequency modelling. The map, shown in the top-left panel of Fig. 4, is smooth across most of the sky and dominated by coherent morphological structures rather than scan-aligned or survey-dependent systematics. The global median spectral index is $\tilde{\beta}_{\rm s} = -3.18$, while a median weighted by synchrotron amplitude yields $\tilde{\beta}_{\rm s} = -3.17$, indicating that the brightest regions dominate the effective synchrotron spectrum inferred by template-fitting approaches. The overall sky dispersion of the spectral index is $\sigma_{\rm sky} \simeq 0.13$. For the 4.76–22.8 GHz baseline, a 5% relative calibration uncertainty from C-BASS alone induces a spectral-index uncertainty of $\sigma_{\beta,\rm cal} \sim 0.045$, while a ~ 1 mK monopole uncertainty at 4.76 GHz contributes $\sigma_{\beta,\rm mono} \sim 0.03$ in bright Galactic-plane regions and up to ~ 0.06 at high Galactic latitudes where the synchrotron brightness temperature is lower. The combined systematic uncertainty is therefore of order ~ 0.05 in the plane and ~ 0.07 at high latitudes, remaining subdominant relative to the observed spatial dispersion. The median posterior standard deviation of the spectral index within the LM95 mask is $\tilde{\sigma}_\beta \simeq 0.16$, indicating that local uncertainties driven by component degeneracies and limited signal-to-noise exceed the calibration-induced systematic

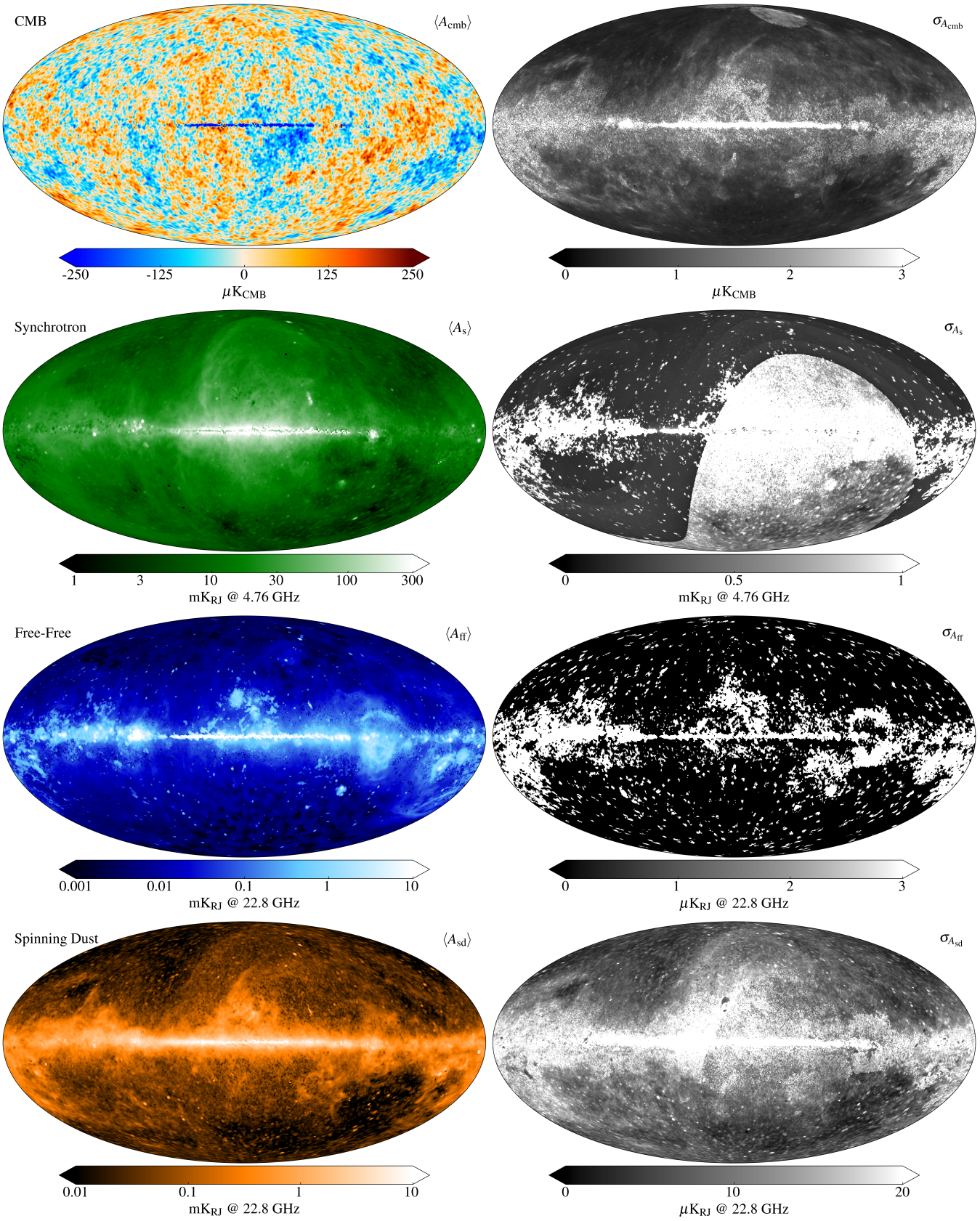

Figure 2. Posterior mean maps (left) and standard deviations (right) for the CMB, synchrotron, free–free, and spinning dust components at their reference frequencies, shown in Galactic Mollweide projection. Foreground means are displayed in logarithmic scale, while the CMB and all standard-deviation maps use linear scale.

floor. A comparison between our synchrotron spectral index map and independent results from the literature is presented in Section 5.1.

In compact regions where free–free emission dominates particularly around bright point sources at low-latitudes, strong degeneracies between components can drive the synchrotron likelihood toward zero, producing small artificial holes in the amplitude map. These pixels are corrected in a post-processing step by replacing near-zero values with the median of valid neighbouring pixels within a 2° radius. This procedure affects only a small fraction of the sky and has no impact on the large-scale synchrotron morphology or on the statistical properties of the spectral index map.

4.1.3 Free–free

The free–free component is intrinsically faint over most of the sky, which makes its separation from synchrotron and spinning dust emission challenging outside lower latitudes. Figure 2 shows the posterior mean free–free amplitude and its associated uncertainty. At high Galactic latitudes, where free–free emission is weak, the solution is dominated by the dust-corrected Hα template. In this regime, prominent structures such as the Gum Nebula and the Eridanus region are robustly recovered, including in the southern sky, and no significant leakage into the other low-frequency components is observed. This indicates that the separation of free–free emission is stable in the Hα-dominated regime at 1° resolution.

The structure of the uncertainty map reflects the hybrid nature of the modelling. Although the FF47 mask formally allows pixel-by-pixel fitting over a larger area, the additional constraint that the fitted free–free brightness must exceed a fraction of the Hα prediction restricts pixel-level fitting to the brightest regions. As a result 78% of the sky is described by the Hα template with a single fitted amplitude, while the remaining 22% is determined through pixel-by-pixel fitting. Consequently, visible uncertainties are confined to the brightest free–free regions where pixel-by-pixel fitting is performed. In the remaining sky, where the free–free emission is described by the Hα template with fixed morphology and amplitude, no posterior uncertainty is sampled for this component. A small number of compact features visible in the free–free amplitude map are likely associated with flat-spectrum radio sources, such as AGNs. Because the present sky model does not include a dedicated spectral component for flat-index sources, their emission is partially absorbed by the free–free term, whose spectral index ($\beta_{\rm ff} \approx -2.1$) is significantly flatter than that of diffuse synchrotron emission. This effect is confined to isolated compact regions and does not impact the large-scale diffuse free–free morphology.

The fractional difference between our free–free solution and the *Planck* 2015 model is shown in the bottom-left panel of Fig. 3. At high Galactic latitudes, the fractional differences appear positively saturated because the *Planck* 2015 free–free model tends toward zero in these regions, whereas the Hα-anchored solution presented here yields well-defined, non-zero values. In contrast, within the Galactic plane the free–free amplitude is systematically lower than in the *Planck* 2015 model. This reduction is a direct consequence of the revised low-frequency modelling: increased flexibility in the synchrotron and spinning dust spectral descriptions reduces the need for free–free emission to absorb spectral mismatches, such that only emission consistent with the characteristic free–free index near −2.1 is retained in that component. In the inner plane ($|b| < 1°$), the free–free amplitude decreases by approximately 10% relative to the *Planck* 2015 model, a trend that is consistent with independent constraints from radio recombination line measurements (Planck Collaboration XXV 2016). Overall, the revised solution yields a cleaner and more physically motivated free–free component in regions of strong component degeneracy. The nature of these degeneracies, however, differs between hemispheres owing to the distinct low-frequency anchors employed in each region. In the southern sky, S-PASS at 2.30 GHz probes a regime where diffuse synchrotron emission strongly dominates over free–free, providing a comparatively clean synchrotron anchor. In the northern sky, C-BASS at 4.76 GHz operates closer to the frequency range where free–free becomes non-negligible in the Galactic plane, increasing the intrinsic synchrotron–free–free degeneracy at that frequency. This effect is mitigated by the inclusion of QUIJOTE data at 11–19 GHz.

4.1.4 Spinning Dust

The final low-frequency foreground component considered in this work is spinning dust emission. Figure 2 shows the posterior mean amplitude at 22.8 GHz together with its uncertainty map. The morphology is dominated by diffuse Galactic structures and closely follows the large-scale dust distribution, indicating that the spatial structure is robustly recovered. A T–T comparison with the *Planck* 2015 solution at $N_{\rm SIDE} = 64$, using the LM95 and PS30 masks, yields a Spearman coefficient of $r_{\rm s} = 0.95$, confirming strong morphological agreement. Our solution is ∼ 5% fainter on average over the full sky and ∼ 25% fainter at high Galactic latitudes (PM61 mask), reflecting a modest renormalisation driven by the revised low-frequency anchoring rather than structural differences. Figure 4 presents the posterior mean peak frequency $\langle \nu_{\rm p} \rangle$ and spectral width w. In the inner Galactic plane, peak frequencies lie predominantly in the range 25–30 GHz, consistent with (Cepeda-Arroita et al. 2025), while surrounding diffuse regions exhibit lower values of 15–20 GHz. In regions with S/N > 10, the typical value is 22 ± 4 GHz, with a median posterior uncertainty of ∼ 1 GHz. The width map is noisier, reflecting limited constraining power, but reproduces broader spectra in the Galactic plane on large angular scales. In the brightest regions, w approaches the lower prior bound, signalling residual degeneracies with other low-frequency components. Allowing w to vary spatially is central to the present modelling: unlike the *Planck* 2015 model, which required two spinning dust components with fixed template shapes, the flexible width parameter captures the observed spectral diversity within a single phenomenological component.

Several structures illustrate the impact of the revised modelling. A diffuse loop, absent in the *Planck* 2015 solution, is clearly detected and spatially correlated with a thermal dust loop in the same region and was first noted in Cepeda-Arroita (2022). Its recovery is primarily enabled by C-BASS, whose frequency proximity to the spinning dust peak improves spectral leverage against synchrotron contamination. The absence of this structure in the earlier model is therefore likely attributable to limited low-frequency anchoring rather than weak intrinsic emission. The region where the Gum Nebula overlaps with the Vela supernova remnant $(l, b) = (260°, -3°)$ does not exhibit enhanced spinning dust amplitude, but instead shows elevated peak frequencies. In the southern sky, spinning dust parameters are constrained mainly by S-PASS and WMAP, whose wide frequency separation limits degeneracy breaking. In contrast, C-BASS provides a closer low-frequency anchor in the north. It therefore remains uncertain whether the higher $\nu_{\rm p}$ inferred in the Gum/Vela region is physically motivated or reflects residual parameter degeneracies.

The ζ Ophiuchi region $(l, b) = (161°, -13°)$, powered by the O-type star ζ Oph and characterised by a prominent H II region and bow-shock structure (e.g. Green et al. 2022), presents additional modelling challenges. Strong free–free emission and complex geometry lead to elevated residuals (see Fig. 5 in Section 4.2) and a comparatively high peak frequency of $\nu_{\rm p} = 31 \pm 7$ GHz. Since bow shocks are

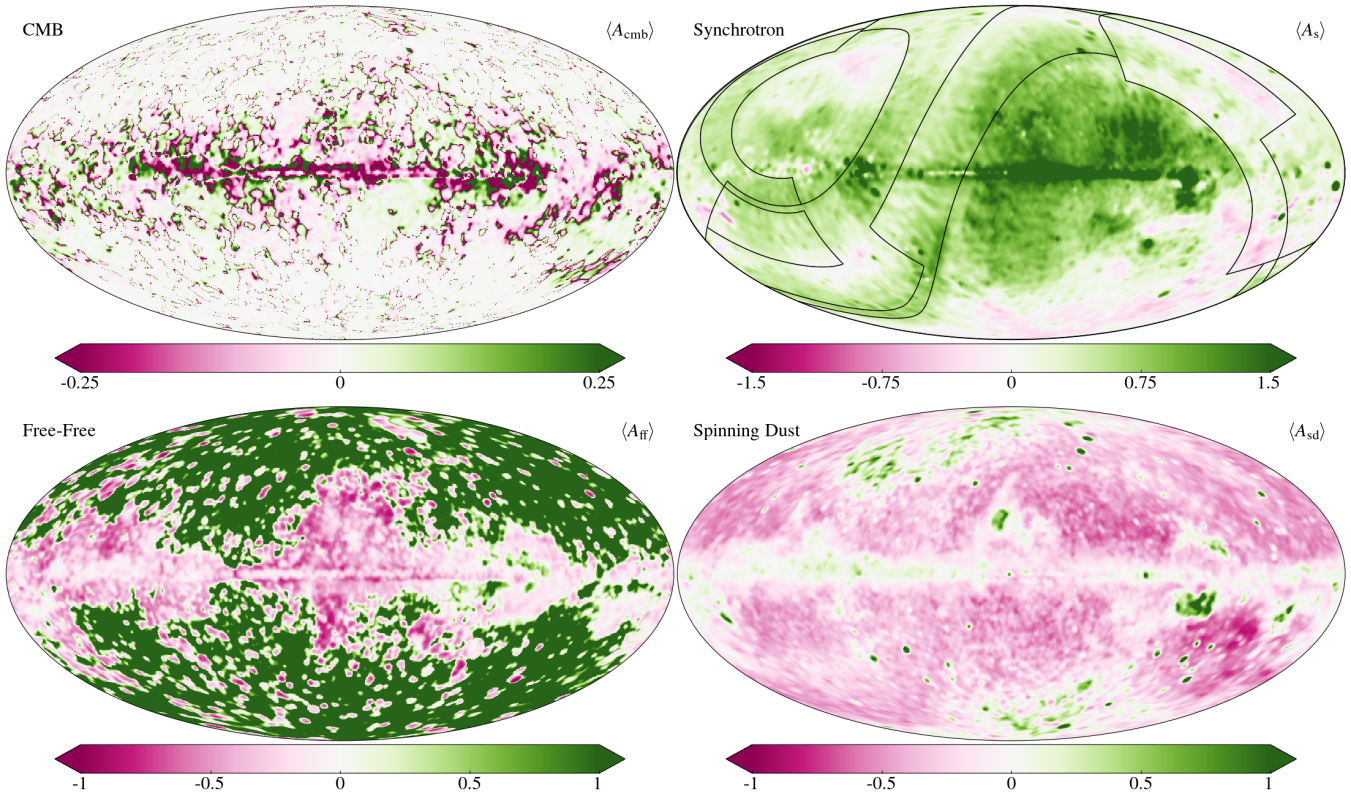

Figure 3. Fractional difference maps at 2° resolution for the CMB and the low-frequency foregrounds. The fractional difference is defined as $(\langle A_{\text{This work}}\rangle - \langle A_{\textit{Planck}\ 2015}\rangle)\,/\langle A_{\textit{Planck}\ 2015}\rangle$. *Top-left map:* CMB in thermodynamic units. *Top-right:* Synchrotron with the Haslam atlas sky zones for the different surveys overlaid for reference (Haslam et al. 1982). *Bottom-left:* Free–free at 22.8 GHz. *Bottom-right:* Spinning dust at 22.8 GHz.

not generally associated with enhanced spinning dust emission, this shift is unlikely to indicate a distinct grain population. Instead, strong free–free emission likely absorbs part of the low-frequency brightness, reducing the fitted spinning dust amplitude and driving the solution toward higher $\nu_{\rm p}$ to preserve the local spectral shape. A similar flattening is observed in the synchrotron spectral index in the same region, consistent with residual component degeneracies.

4.2 GOODNESS-OF-FIT

The goodness-of-fit analysis follows the same methodology adopted in the *Planck* 2015 model, allowing for a direct and consistent comparison. Residual maps are defined as $\mathbf{r}_\nu = \mathbf{d}_\nu - \mathbf{s}_\nu$, where $\mathbf{d}_\nu$ denotes the observed data map at frequency ν and $\mathbf{s}_\nu$ is the corresponding best-fitting sky model, including all astrophysical components and instrumental corrections. The residual maps are shown in Figs. 5 and 6, while quantitative goodness-of-fit metrics are summarised in Table 3. As in the previous analysis, residuals are evaluated in brightness temperature units at a common angular resolution of 1°. The model provides an excellent fit over most of the sky, with residuals at high Galactic latitudes generally consistent with instrumental noise. Residuals in the *Planck* HFI channels are not shown explicitly, as their behaviour is essentially unchanged relative to the *Planck* 2015 solution. The use of Cosmoglobe-reprocessed WMAP and LFI maps removes the large-scale CMB quadrupole residual present in the original *Planck* 2015 LFI products, reducing typical LFI residual amplitudes from $\sim \pm 10\,\mu$K to $\sim \pm 5\,\mu$K. In the Galactic plane, residuals in the WMAP Q- and V-bands are reduced, while modest increases are observed in K-band and LFI 30 GHz in regions overlapping with QUIJOTE coverage. These changes reflect the revised balance of low-frequency foreground components when S-PASS and C-BASS are included. At the lowest radio frequencies, S-PASS and C-BASS dominate the fit, yielding residuals well below their thermal noise RMS, as expected for channels that strongly constrain the model in their respective frequency ranges.

The statistical goodness-of-fit is quantified through the χ^2 map shown in the top panel of Fig. 6, constructed from the Gaussian likelihood and summed over all frequency channels. As in the *Planck* 2015 analysis, the effective number of degrees of freedom cannot be determined by simply counting parameters, owing to informative priors, spatial smoothing, and spatially constant instrumental parameters. Instead, we estimate the effective degrees of freedom by fitting a scaled χ^2 distribution to the empirical χ^2 distribution in clean regions of the sky. We adopt the conservative PM61 mask for this purpose and obtain an effective distribution corresponding to $\nu \simeq 20$ degrees of freedom with a correlated-noise scaling factor of 1.09, identical to the value found in the *Planck* 2015 model. Since 30 frequency channels enter the fit, this implies an effective number of $30 - 20 = 10$ free parameters per pixel, compared to 13 parameters in the formal model. The combined action of priors therefore removes approximately three degrees of freedom, confirming that the solution remains predominantly data-driven. Based on this fit, we define the primary confidence mask LM95 by thresholding the χ^2 map, smoothed with a 1° Gaussian kernel, at $\chi^2 = 50$, corresponding to the upper tail of the distribution. This mask excludes approximately 5% of the sky and defines the region where the likelihood is considered reliable. The LM95 mask is shown as the red contours in the top panel of Fig. 6.

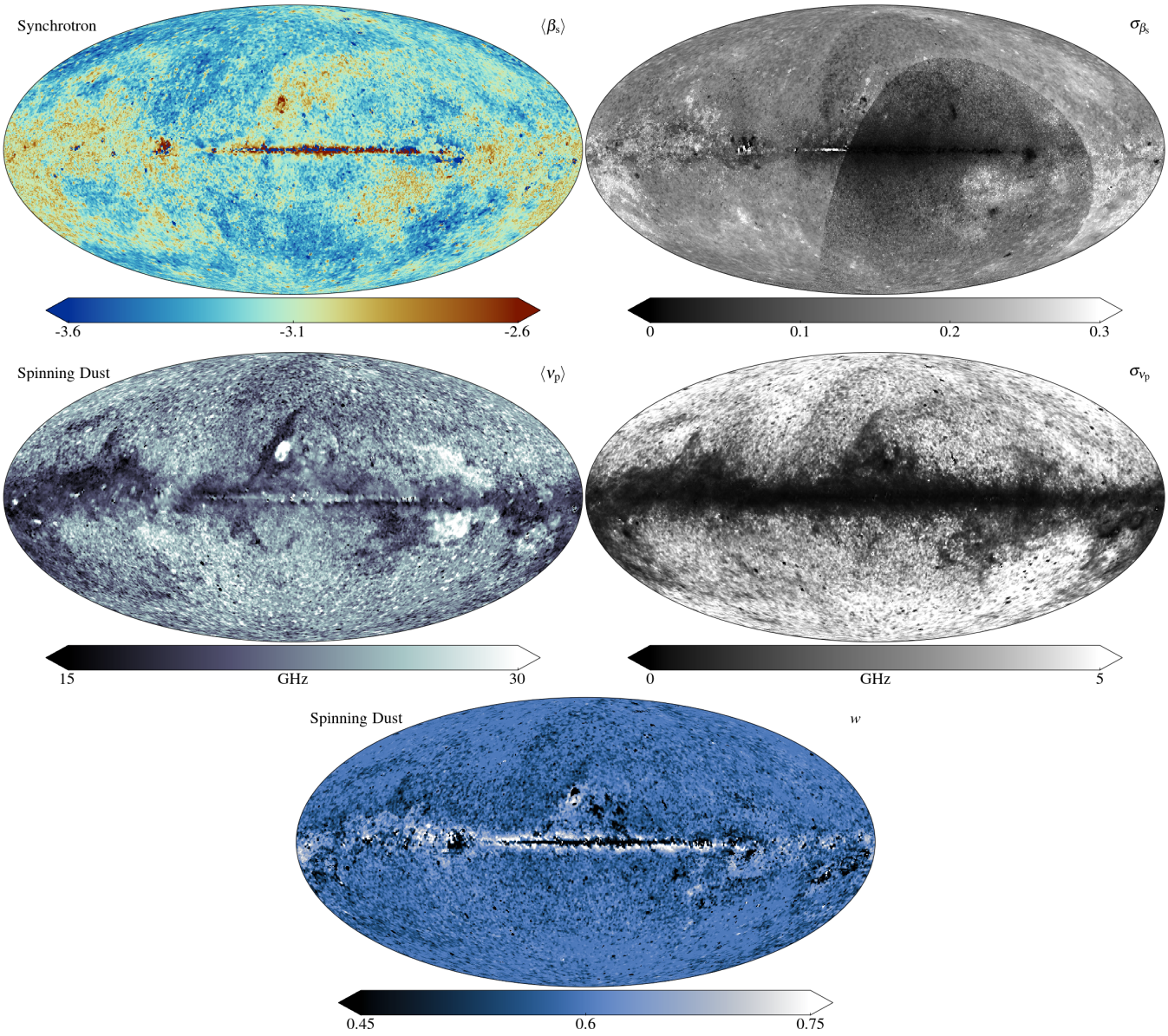

Figure 4. Posterior maps (left column) and corresponding posterior standard deviations (right column) for the synchrotron spectral index β_s, the spinning dust peak frequency ν_p, and the spinning dust width w. The synchrotron spectral index and peak frequency are shown as posterior means, while the spinning dust width corresponds to its maximum-likelihood solution.

Compared to the *Planck* 2015 model, this represents an increase of $\sim 3\%$ in usable sky fraction.

Additional diagnostics are provided by the residual angular power spectra and by channel-by-channel statistics. The bottom panel of Fig. 6 shows the residual C_ℓ spectra evaluated in the LM95 region, compared to the CMB and low-frequency foregrounds at 30 GHz power spectrum in the same sky fraction. Residual power remains at least two orders of magnitude below the CMB signal for multipoles $\ell < 192$, demonstrating that the component separation is clean at the angular scales targeted in this work. Table 3 lists, for each channel, the RMS of the residual map outside the LM95 mask and its ratio to the corresponding instrumental noise RMS. For most channels this ratio is close to unity, indicating that residuals are consistent with noise not only in an integrated χ^2 sense but also on a channel-by-channel basis. Compared to the *Planck* 2015 model, S-PASS and C-BASS now dominate the synchrotron constraints at low frequencies, while the proximity of these surveys to WMAP K-band reduces the extent to which K-band alone dominated the low-frequency foreground solution in the earlier analysis. This leads to a modest redistribution of residual power across low-frequency channels without degrading the overall fit quality. Median fractional residuals within the LM95 region are below 0.2% for all HFI channels, below 0.5% for all LFI channels, below 1.5% for all WMAP channels, and below 5% for QUIJOTE channels, consistent with the adopted calibration uncertainties.

Overall, the goodness-of-fit diagnostics demonstrate that the revised model provides a statistically consistent description of the temperature sky. Residuals are noise-dominated over more than 95% of the sky, the effective number of degrees of freedom matches that of the *Planck* 2015 model, and the inclusion of modern low-frequency surveys improves the physical consistency of the solution without introducing

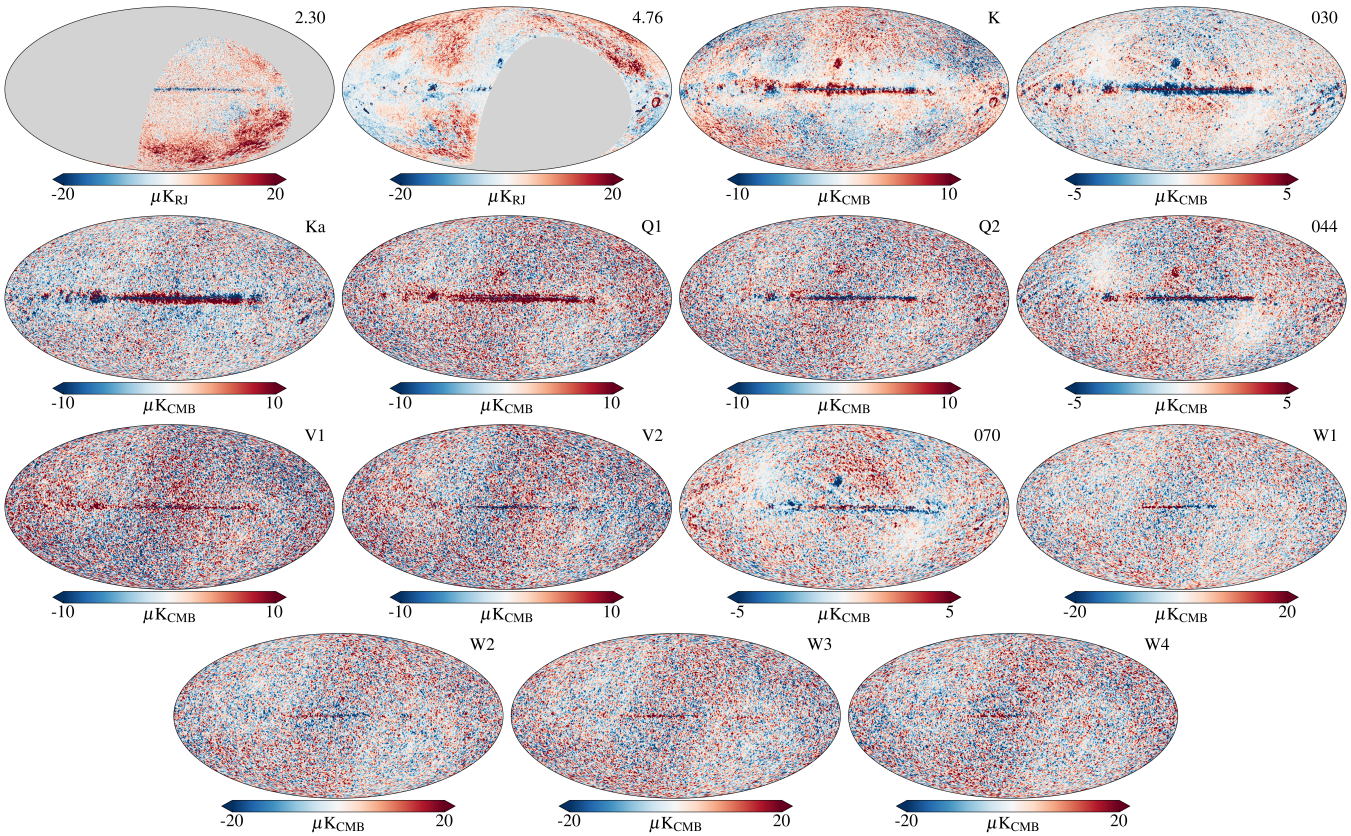

Figure 5. Residual maps, $d_\nu - s_\nu$, for each detector data set included in the baseline joint S-PASS, C-BASS, *Planck* LFI and WMAP. All panels employ linear colour scales. The label in the top-right corner of each panel indicates the frequency channel.

significant degradations in fit quality. These results confirm that the revised low-frequency modelling yields a robust component separation suitable for scientific interpretation.

4.3 ALL-SKY MAP AT 4.76 GHz

Using the parametric model derived in this work, we construct an all-sky total-intensity map at 4.76 GHz. While the model can in principle be evaluated at any frequency, 4.76 GHz represents the lowest frequency at which the solution is directly constrained over the full sky. Below this frequency, no northern-sky data are available, and any extrapolation increasingly relies on the assumed spectral model rather than on direct observational constraints. The resulting all-sky map, together with its associated uncertainty estimate, is shown in Fig. 7. The uncertainty map is obtained by propagating the posterior uncertainties of the individual components and summing them in quadrature after evaluating each component at 4.76 GHz. At this frequency, the total intensity is dominated by synchrotron emission, with secondary contributions from free–free emission and, in selected regions, spinning dust, while thermal dust is negligible. It is important to note that the northern sky at 4.76 GHz is directly constrained by C-BASS observations, whereas the southern sky is obtained by extrapolating the S-PASS 2.30 GHz map to 4.76 GHz using the pixel-dependent spectral indices derived from the global parametric fit. As a consequence, the posterior standard deviation is systematically larger in the southern hemisphere, as visible in Fig. 7, reflecting the additional spectral extrapolation uncertainty.

A direct comparison with the *Planck* 2015 model evaluated at the same frequency is presented through a T–T analysis shown in Fig. 8. The comparison is performed at N_{SIDE} 64, masking the Galactic plane with the PM61 mask and excluding compact sources using the PS30 mask. The two models are highly correlated morphologically, confirming that they trace the same large-scale Galactic structures. However, the best-fitting slope departs significantly from unity, indicating that the *Planck* 2015 solution underestimates the total sky brightness at 4.76 GHz by $\sim 55\%$ relative to the present model, driven primarily by differences in the synchrotron component. The T–T distribution shows a clear bifurcation around the best-fitting relation: the upper branch is dominated by Galactic-plane pixels, while the lower branch is associated with high-latitude structures, most prominently the North Polar Spur. This behaviour reflects the impact of allowing spatial variations in the synchrotron spectral properties across the sky, rather than assuming a spatially uniform spectral index as in the *Planck* 2015 model. In the northern sky, the resulting map therefore closely follows the original C-BASS observations. The main enhancement occurs in the southern hemisphere: instead of adopting a spatially uniform rescaling of S-PASS with monopole and dipole corrections, the present approach propagates a pixel-dependent synchrotron spectral index derived from the global parametric fit. This allows spatial variations in spectral shape to be consistently mapped to 4.76 GHz, yielding a more physically realistic representation of the large-scale emission.

A direct comparison with the *Planck* 2015 model evaluated at the same frequency is presented through a pixel-by-pixel T–T analysis shown in Fig. 8. The comparison is performed at N_{SIDE} 64, masking the Galactic plane with the PM61 mask and excluding compact sources using the PS30 mask. The two models are highly correlated morphologically, confirming that they trace the same large-scale Galactic

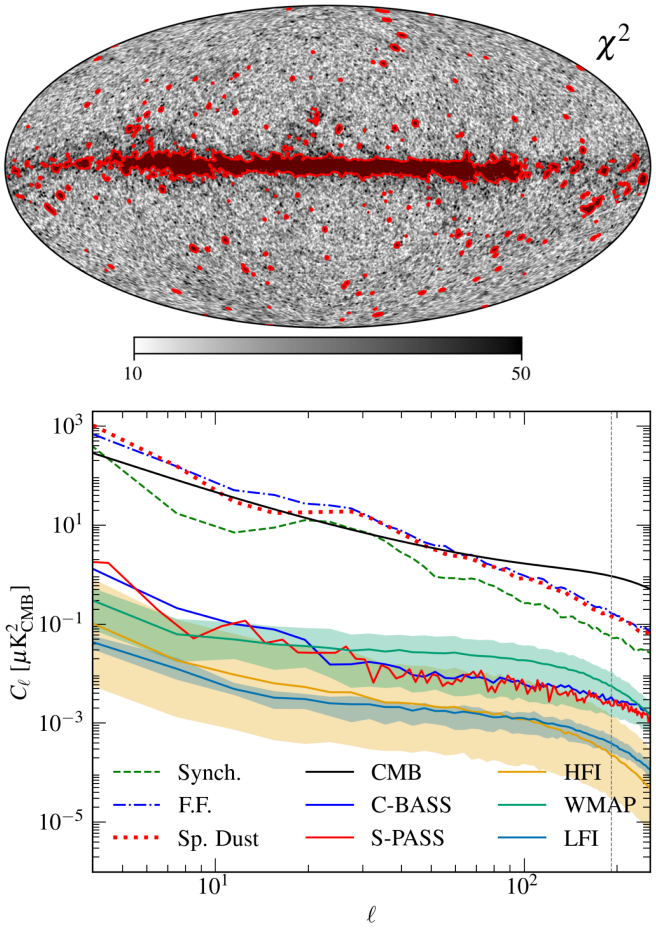

Figure 6. Goodness-of-fit diagnostics for the model. *Top:* Map of χ^2 per pixel at 1° angular resolution. Red contours indicate the LM95 mask used in the analysis. *Bottom:* Angular power spectra of the residual maps for each frequency channel after subtraction of the best-fitting model. For each instrument class (LFI, HFI, and WMAP), the shaded regions show the minimum and maximum residual power at each multipole, while the solid lines indicate the corresponding mean spectra. The black curve shows the CMB angular power spectrum for reference. The dashed green, dash-dotted blue, and dotted red curves indicate the synchrotron, free–free, and spinning dust power spectra, respectively, evaluated at 30 GHz.

structures. However, the best-fitting slope departs significantly from unity, indicating that the *Planck* 2015 solution underestimates the total sky brightness at 4.76 GHz by ∼ 55% relative to the present model, primarily due to differences in the synchrotron component. The T–T distribution exhibits a clear bifurcation with the upper branch is dominated by high-latitude emission associated with the North Polar Spur, while the lower branch is primarily linked to regions closer to the Galactic centre. This separation reflects the impact of allowing spatial variations in the synchrotron spectral properties across the sky, rather than enforcing a spatially uniform spectral index as in the *Planck* 2015 model. As a result, the reconstructed map closely follows the original C-BASS observations in the northern sky, while in the southern hemisphere it is an enhanced solution by propagating spectral variations from the global parametric fit—rather than applying a uniform rescaling of S-PASS with monopole and dipole corrections. This yields a more physically realistic representation of the large-scale emission at 4.76 GHz.

All-sky maps constructed in this way are particularly valuable for sky-simulations such as PSM, PySM, and related models. The

Table 3. Goodness-of-fit statistics.

		RMS outside LM95		Frac. res. inside
	Map	[μK] [a]	$\sigma_\nu^{\rm res}/\sigma_\nu^{\rm inst}$ [b]	LM95 [%] [c]
S-PASS	2.30	3.42	0.01	0.00
C-BASS	4.76	4.70	0.03	0.00
QUIJOTE	11.1	...	...	4.72
	12.9	...	...	4.53
	16.8	...	...	3.41
	18.8	...	...	4.87
WMAP	K	3.73	0.62	0.12
	Ka	4.59	1.00	0.86
	Q1	5.33	0.95	0.67
	Q2	5.10	0.98	0.54
	V1	6.39	0.84	1.07
	V2	5.76	0.89	0.92
	W1	8.46	0.84	1.30
	W2	9.99	0.89	1.52
	W3	10.24	0.85	1.47
	W4	10.35	0.92	1.51
Planck	28.4	1.52	0.66	0.16
	44.1	2.27	0.84	0.36
	70.3	1.96	0.94	0.37
	100-ds1	0.67	0.75	0.01
	100-ds2	0.58	0.72	0.01
	143-ds1	0.72	1.02	0.07
	143-ds2	0.68	0.98	0.08
	143-5	1.02	1.14	0.14
	143-6	1.18	1.08	0.10
	143-7	1.07	1.07	0.09
	217-1	1.71	0.95	0.06
	217-2	1.98	1.04	0.08
	217-3	1.64	0.96	0.07
	217-4	1.75	0.97	0.05
	353-ds2	3.89	1.11	0.02
	353-1	1.49	0.33	0.01
	545-2	9.32 [d]	0.93	0.14
	545-4	9.55 [d]	0.95	0.13
	857-2	1.24 [d]	0.12	0.00

Notes: [(a)] RMS residual outside the 95% `Commander` likelihood mask for each channel except for QUIJOTE channels since their masks are about the coverage of LM95. [(b)] Same as [(a)], but normalised with respect to the instrumental noise RMS listed in Table 1. [(c)] Median fractional residual in the complementary 5% of the sky, covering the Galactic plane region. [(d)] Unit is kJy/sr.

4.76 GHz map provides a physically motivated intermediate-frequency anchor between traditional low-frequency radio surveys and microwave data, substantially reducing the need for long extrapolations from 408 MHz or for purely phenomenological prescriptions. As such, it offers a robust input for simulations of Galactic foregrounds in the radio-to-microwave transition regime. Although 4.76 GHz is the lowest frequency at which the present solution is directly constrained over the entire sky, extrapolation of the model to slightly lower frequencies remains feasible. In the northern sky, no data below 4.76 GHz are included in the present parametric fit, and therefore predictions at lower frequencies rely on spectral extrapolation of the fitted components

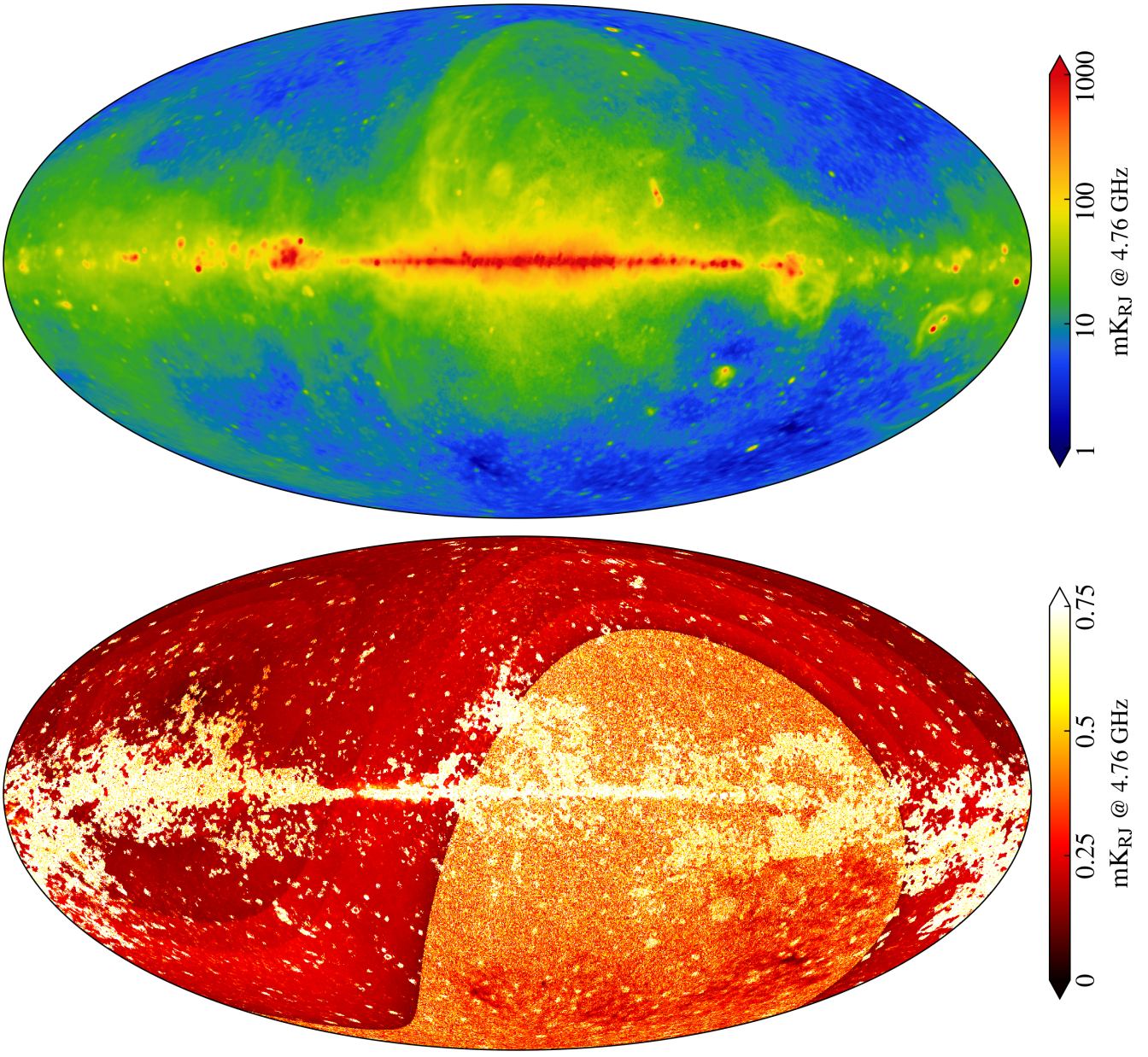

Figure 7. All-sky total-intensity map at 4.76 GHz constructed from the posterior averages presented in this work, shown together with its corresponding uncertainty map. The map is evaluated at 1° angular resolution and represents the sum of the synchrotron, free–free, and spinning dust components at this frequency.

rather than on additional observational constraints. Given that the inferred synchrotron curvature is small down to frequencies of order 1 GHz, approximate all-sky maps can be constructed at 2.30 GHz within the adopted spectral model.

5 DISCUSSION

This section addresses the physical interpretation of the reconstructed foreground components. The recovered maps and spectral parameters are compared with independent literature results, and the main limitations related to data coverage, calibration, and modelling assumptions are discussed. The analysis presented here is intentionally brief. A more detailed investigation of each foreground component and a comprehensive comparison with independent studies will be the subject of future work.

5.1 LOW FREQUENCY SPECTRAL INDEX

We compare the spectral index maps derived from our model with independent reconstructions from the literature, acknowledging that differences in frequency coverage and survey systematics limit the extent to which detailed morphological agreement can be expected. Together with the synchrotron spectral index β_s, spectral indices for the total sky emission can also be predicted from our model by evaluating the sky solution at two frequencies. Appendix C presents examples of such spectral index maps. We compare our synchrotron spectral index map with the Irfan (2023) map between 0.408–23 GHz

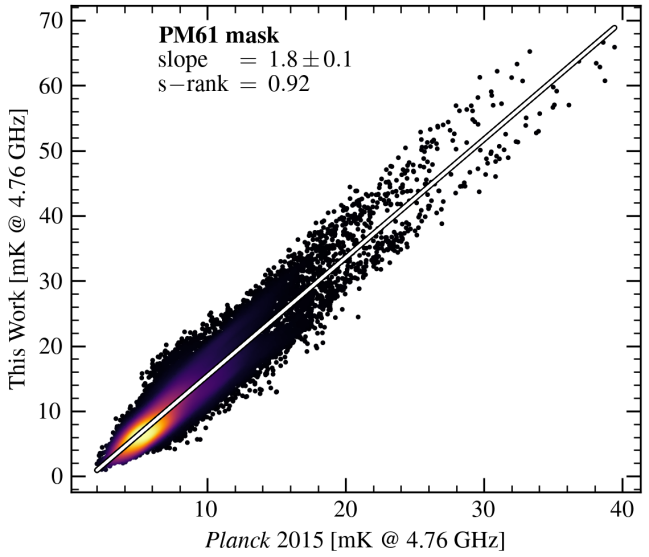

Figure 8. T–T plot between the *Planck* 2015 model and the model presented in this work at 4.76 GHz, evaluated at N_{SIDE} 64 using the PM61 mask and the PS30 mask. The line shows the best-fitting linear relation.

and with the Irfan & Puglisi (2025) map, by extrapolating their β_s map from 43 MHz to 4.76 GHz using their curvature map. We also compare a spectral index map from our model between 2.30–22.8 GHz (noting that this involves extrapolation in the northern sky) with the Giardino (2009) map (0.408–22.8 GHz). Finally, we compare a spectral index map from our model between 2.30–4.76 GHz with the Finkbeiner (2009), Giardino et al. (2002) and Platania et al. (2003) maps (0.408–2.30 GHz). All comparisons are performed through T–T analyses after smoothing to a common 2° resolution and degrading to N_{SIDE} 32. We adopt the PM61 and LM95 masks, representing large-scale regions with and without the Galactic plane, where the model residuals are low (see Section 4.2). Point sources are masked using the PS30 mask. The resulting Spearman rank coefficients are listed in Table 4. All literature spectral index maps show only weak pixel-by-pixel correlations with our solution, as the Spearman coefficients remain low in every case, indicating that the detailed spatial structure of the inferred spectral index differs substantially between reconstructions. This behaviour arises because spectral index maps are second-order quantities that amplify large-scale systematics such as zero-level uncertainties, residual striping, and calibration errors present in the input surveys. For illustration, calibration uncertainties alone can induce spectral-index uncertainties of order $\sigma_\beta \sim 0.07$ for a 408–2.3 GHz baseline, even before accounting for zero-level offsets, residual striping, or other large-scale systematics. Because the spectral index depends on logarithmic intensity ratios, it is intrinsically sensitive to small multiplicative and additive errors, which inevitably affect all β reconstructions to some degree. In our case, after propagating calibration, monopole, and other systematic uncertainties included in the noise model, the resulting spectral-index uncertainty reaches at most ~ 0.07 at high Galactic latitudes. Since many literature products rely heavily on legacy low-frequency surveys, the resulting index morphologies inherit these artefacts and are dominated by systematics rather than by physical synchrotron structure.

The map showing the closest agreement with our reconstruction is that of Giardino (2009), which includes WMAP K-band data in its spectral index estimation. This is expected since the K-band lies in the same frequency regime that anchors our synchrotron solution,

Table 4. Spectral index T–T plot Spearman rank coefficients in the PM61 and LM95 regions.

Reference [a]	Freq. range	r_s (PM61)	r_s (LM95)
Irfan & Puglisi (2025) [b]	@ 4.76 GHz	0.12	0.29
Irfan (2023) [b]	0.408–23 GHz	0.10	0.08
Giardino (2009) [c]	0.408–23 GHz	0.30	0.62
Finkbeiner (2009) [d]	0.408–2.3 GHz	0.01	0.01
Platania et al. (2003) [d]	0.408–2.3 GHz	0.11	0.21
Giardino et al. (2002) [d]	0.408–2.3 GHz	0.52	0.69

Notes: [(a)] Spectral indices maps from this work are on the x-axis and from external works are on the y-axis. [(b)] Compared against the synchrotron spectral index map at 4.76 GHz from this work. [(c)] Compared against the spectral index at 2.30–22.8 GHz generated from the model of this work. [(d)] Compared against the spectral index at 2.30–4.76 GHz generated from the model of this work.

whereas the other maps used here rely predominantly on lower-frequency surveys in a regime not directly constrained by our model. Differences therefore arise not only from survey systematics but also from the effective frequency baseline over which the index is defined and from the treatment of spectral curvature. In our case, the spectral index is inferred within a multi-frequency parametric framework using modern surveys with improved calibration and reduced large-scale artefacts, suppressing scan-related patterns. Table 4 should therefore be interpreted as a diagnostic of methodological and dataset differences rather than as a measure of physical disagreement. The weak correlations confirm that low-frequency spectral index maps remain strongly systematics-limited, and that the inferred index distribution is highly sensitive to survey choice, frequency coverage, and modelling assumptions.

5.2 DUST CORRELATION

The spatial correlation between spinning dust and thermal dust emission reflects the link between electric-dipole emission from rapidly rotating very small grains and the overall dust column density. We quantify this relation through a T–T analysis between the spinning dust amplitude at 22.8 GHz, A_{sd}, and the thermal dust amplitude at 545 GHz, A_d, derived from our component-separation model. The analysis is performed at $N_{SIDE} = 64$, masking compact sources with the PS30 mask and applying the same S/N > 3 mask used in Planck Collaboration et al. (2016). A linear fit yields a slope of 74 ± 7 μK/MJy sr^{-1} and a Spearman rank coefficient of $r_s = 0.93$, confirming a strong monotonic correlation. We also compare A_{sd} with the dust optical depth τ_{353} (Planck Collaboration XI 2014), obtaining $r_s = 0.93$ and a best-fitting slope of $(12 \pm 1) \times 10^6$ μK/τ_{353}. Since τ_{353} traces dust column density more directly than A_d, being less sensitive to temperature variations, this provides a complementary test of whether spinning dust scales with dust mass rather than dust heating conditions. The slopes reported in Planck Collaboration XXV (2016) are slightly lower than those obtained here because their correlation was computed using only the lower-frequency spinning dust component of the *Planck* 2015 model. When the sum of both spinning dust components in the *Planck* 2015 model is used instead, the inferred slopes increase and become slightly larger than ours by approximately 5%, consistent with the relative amplitude difference between the two solutions.

Despite the strong global linear correlation described above, the T–T distribution departs from strict linearity at high thermal dust

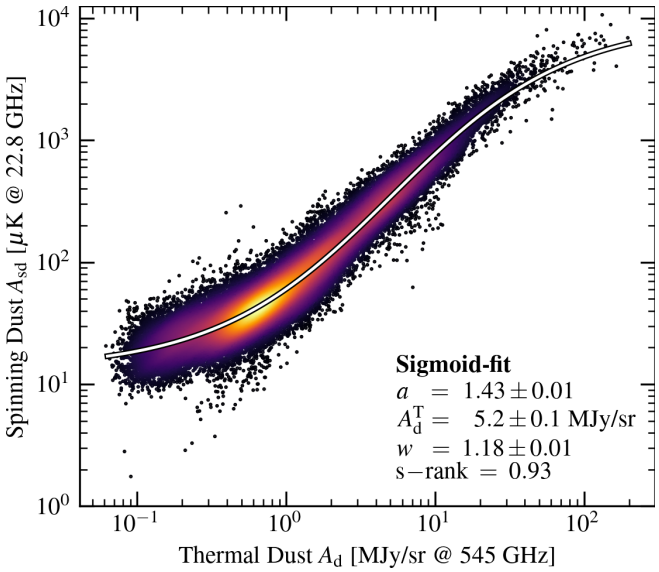

Figure 9. T–T plot between the spinning dust amplitude at 22.8 GHz and the thermal dust amplitude at 545 GHz, evaluated at a common angular resolution and N_{SIDE} 64. Pixels are selected using the S/N > 3 mask (Planck Collaboration XXV 2016) and the PS30 mask. The colour scale indicates the density of the scatter points, while the solid curve shows the best-fitting hyperbolic-tangent model.

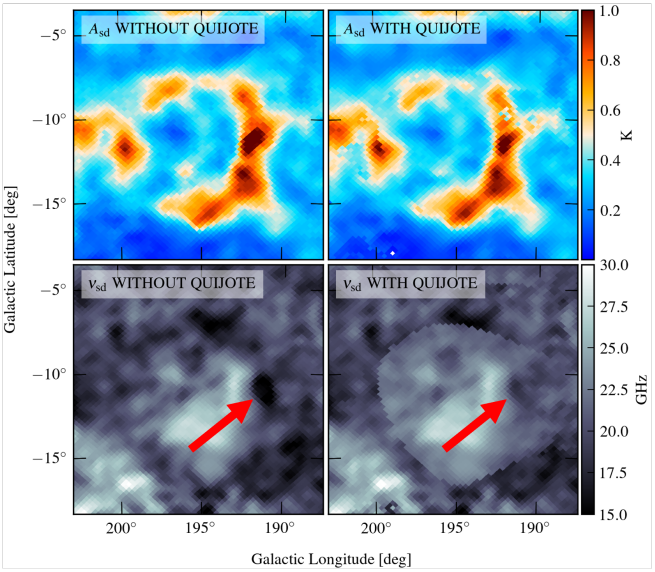

Figure 10. Comparison of spinning dust parameters in the λ Orionis region. *Top row*: spinning dust amplitude A_{sd} at 22.8 GHz without (left) and with (right) QUIJOTE data included in the fit. *Bottom row*: corresponding peak frequency maps ν_{sd} without (left) and with (right) QUIJOTE. All panels show the same sky region in Galactic coordinates. The red arrow marks the position of the B30 cloud for reference.

amplitudes, where the emissivity decreases. This behaviour was already visible in Planck Collaboration et al. (2016) and reflects reduced spinning dust efficiency in regions of high dust column density. To capture this transition, we model the T–T relation in logarithmic space using a sigmoid form based on a hyperbolic tangent,

$$\log A_{sd} = a \tanh\left(\frac{\log A_d - \log A_d^T}{w}\right) + b, \quad (2)$$

which describes two asymptotic regimes connected by a smooth transition and provides a more realistic representation of the full dynamic range than a single linear slope. The fitted transition parameter is $A_d^T = 5.2 \pm 0.1$ MJy sr^{-1}, which marks the characteristic thermal dust amplitude where the spinning dust emissivity begins to flatten. The fit yields χ^2/dof = 133.7, significantly larger than unity, as expected for a phenomenological model that does not attempt to capture the full intrinsic scatter of the data. Introducing an additional dispersion term to account for intrinsic variation requires a fractional scatter of $\sigma_{scatter} = 1.37$, corresponding to a 37% dispersion. Physically, this transition scale indicates the dust column density above which environmental effects modify the small-grain population: at low to intermediate column densities, spinning dust efficiently traces the abundance of very small grains, while at higher column densities, grain growth, coagulation, and mantle formation reduce the relative population of the smallest rapidly rotating particles responsible for electric-dipole emission. Thermal dust emission continues to scale with total dust mass, leading to a decrease in the effective A_{sd}/A_d ratio beyond the transition. The hyperbolic-tangent model therefore provides a compact phenomenological description of how spinning dust efficiency evolves with dust environment while preserving the strong overall dust correlation.

5.3 ROLE OF 10–20 GHz DATA IN CONSTRAINING FOREGROUND SPECTRA

The 10–20 GHz range is a regime where degeneracies between synchrotron, free–free, and spinning dust parameters are particularly strong, since the spectral contributions of these components overlap and their relative slopes differ most sensitively on the rising side of the spinning dust spectrum. This frequency window is therefore critical for separating components and for constraining the peak frequency and width of spinning dust. In our analysis, QUIJOTE data are used exclusively in the Galactic plane, where they contribute to constraining the spectral parameters of the emission components. Even with reduced statistical weight, the QUIJOTE channels provide anchoring in a frequency range that is otherwise sparsely covered, thereby reducing degeneracies in the component separation solution. Frequencies below this range mainly constrain synchrotron behaviour, while those above 20–30 GHz probe the declining side of the spinning dust spectrum together with free–free emission. A clear illustration is provided by the B30 cloud in the λ Orionis region in Fig. 10. When QUIJOTE data are excluded, the fit between C-BASS and WMAP/*Planck* channels is weakly constrained on the rising side of the spinning dust spectrum, and the solution converges to a peak frequency near ∼ 12 GHz. After including the 11 and 13 GHz QUIJOTE channels, even with the 5% calibration error added to the RMS uncertainties, the spectral solution shifts toward a peak near ∼ 23 GHz, consistent with previous measurements of the region (Harper et al. 2025; Cepeda-Arroita et al. 2025). This example shows that coverage in the 10–20,GHz range is essential for breaking degeneracies between synchrotron, free–free, and spinning dust, enabling more robust constraints on their spectral parameters and, potentially, on the width of the spinning dust spectrum. It underscores the need for future full-sky surveys in this frequency regime.

5.4 MODEL LIMITATIONS

Although the model presented here provides an improved description of the low-frequency Galactic sky relative to previous analyses, its interpretation remains limited by the available data, frequency coverage, and adopted parametric assumptions. A major advance of this work is the replacement of the traditional 408 MHz anchor with modern surveys closer to the CMB frequency range (i.e. S-PASS, C-BASS, and QUIJOTE) not needing use a curved synchrotron model to connect widely separated frequency regimes. Nevertheless, the 10–40 GHz interval remains intrinsically challenging, as synchrotron, free–free, and spinning dust contribute comparable power and their spectra partially overlap. Even with these data, the separation between synchrotron spectral behaviour, free–free emission, and the rising side of the spinning dust spectrum is not uniquely determined in all regions. The inferred spinning dust peak frequency and width, as well as the relative partition of emission between components, therefore depend to some degree on the adopted spectral forms and priors, particularly in areas with incomplete 10–20 GHz coverage or low S/N. These parameters should be regarded as effective descriptors of the observed spectrum rather than direct measurements of intrinsic grain properties. Fully breaking these residual degeneracies requires full-sky surveys in the S-PASS, C-BASS, and QUIJOTE frequency ranges, which would anchor the synchrotron and spinning dust spectra across the critical transition regime.

Additional limitations arise from survey characteristics, frequency coverage, and calibration uncertainties. The QUIJOTE maps, while crucial for constraining spectral behaviour in the Galactic plane, do not provide full-sky coverage at 10–20 GHz, and large angular scales are partially suppressed by map-making filtering. Outside the plane, the spinning dust spectrum is therefore driven primarily by WMAP and *Planck* LFI data together with model priors, and constraints in this range remain indirect. At lower frequencies, maps below 4.76 GHz in the northern sky rely on model extrapolation, since no data are used there in this work. Although strong spectral curvature is not expected down to a $\sim$ 1 GHz, such extrapolations are not directly data-driven and may introduce biases in regions with complex spectral behaviour. Furthermore, absolute zero levels are not perfectly known, and the derived synchrotron spectral index is sensitive to the adopted relative offsets between frequency channels. Unlike classical flux-based spectral index estimates or T–T analyses that explicitly remove background levels, the parametric fit operates on maps containing residual large-scale offsets, and small zero-level mismatches can therefore propagate into the recovered spectral parameters. In particular, for the synchrotron spectral index β_s, these effects increase the uncertainty to $\sigma_{\beta_s} \sim 0.05$ in the Galactic plane and up to ~ 0.07 at high Galactic latitudes.

The adopted component models also introduce intrinsic limitations. Synchrotron emission is described by a single power-law SED per pixel over the fitted range. This becomes particularly limiting at frequencies above the spinning-dust peak, where the declining side of the spinning-dust spectrum has an effective spectral index of approximately $\beta \approx -3.1$, similar to that of synchrotron emission. In these frequencies the spectral shapes become difficult to distinguish, and residual degeneracy between synchrotron and spinning dust can lead to leakage between the two components, especially in regions where the overall spectrum is relatively flat. Free–free emission outside the Galactic plane is largely template-driven through Hα, making the solution sensitive to dust-extinction corrections and Hα scattering, while inside the plane the separation relies on fixed spectral assumptions and an external electron-temperature map, leaving residual degeneracies with other components. The spinning dust spectrum is represented by a single log-normal form, which is flexible enough for the available data but remains a phenomenological description. Real spinning dust likely arises from multiple environments, and the fitted peak frequency and width do not map uniquely onto specific grain populations.

Finally, the analysis is performed at a common angular resolution of 1° FWHM, so compact H II regions and small-scale spinning dust sources are beam-diluted and their parameters represent large-scale averages rather than intrinsic source properties. Compact synchrotron-dominated sources with unusually flat spectra, such as Tau A, are not well described by the diffuse synchrotron model and can produce localised residuals in amplitude and spectral index maps. Pixel-by-pixel fitting also does not fully correct for beam-shape differences between surveys. Residual beam asymmetries and scan-dependent systematics lead to small morphological mismatches of point sources between channels, producing characteristic quadrupolar residual patterns around bright sources. In addition, transitions at the boundaries between surveys with different sky coverage can introduce slight morphological discontinuities in the reconstructed component maps. In addition, the solution depends on the adopted priors within `Commander`, and in low S/N regions posterior distributions are partially prior-driven. The model provides a self-consistent large-scale description of the sky, but its parameters should be interpreted with these data, model, calibration, and prior dependencies in mind.

6 CONCLUSION

We have presented a new all-sky model of low-frequency diffuse Galactic emission describing the regime where synchrotron, free–free, and spinning dust dominate the sky brightness. This work extends the *Planck* 2015 model by incorporating modern surveys that anchor the sky closer to the CMB frequency range: S-PASS, C-BASS, and QUIJOTE (in the Galactic plane). We also used the Cosmoglobe reprocessed WMAP and *Planck* LFI maps with improved large-scale calibration, replacing earlier versions of these data sets. The main advance is the re-anchoring of the synchrotron component at C-band frequencies, replacing the traditional need on the Haslam 408 MHz map. The recovered spectral index distribution shows flattening toward the Galactic plane and steepening at high latitudes, consistent with variations in the cosmic-ray electron population, and leads to a redistribution of power between synchrotron, free–free, and spinning dust relative to earlier models.

The spinning dust component remains strongly correlated with thermal dust, but its total power is reduced compared to the *Planck* 2015 reconstruction as a consequence of the revised synchrotron solution. The peak frequency map exhibits coherent large-scale structure, while the spectral width remains weakly constrained outside bright regions. Free–free emission is more stable at high latitudes through the use of Hα as a tracer, although extinction corrections and degeneracies in the Galactic plane remain sources of uncertainty. QUIJOTE data provide additional constraints in the 10–20 GHz range in selected regions, but the dominant structural improvements arise from the revised low-frequency anchoring. A key product of this work is a new all-sky total-intensity map at 4.76 GHz, which provides a reference tracer of diffuse synchrotron emission between classical radio surveys and microwave data. The component maps also provide updated inputs for sky simulations and foreground modelling, reducing dependence on large extrapolations from very low frequencies and improving the description of the transition between radio and microwave emission.

Residual limitations remain. Degeneracies between synchrotron, free–free, and spinning dust persist in the 10–40 GHz regime, and

absolute zero-level uncertainties, incomplete frequency coverage, and parametric assumptions affect the recovered parameters. Compact sources with unusual spectra and beam mismatches introduce localised residuals. Addressing these issues requires future full-sky surveys in the 1–20 GHz range with improved calibration and large-scale sensitivity. Within these limits, this work establishes an updated reference description of the low-frequency diffuse Galactic sky and defines a baseline for studies of Galactic emission, CMB foreground separation, and sky simulation, while identifying the frequency range where further observational progress is required.

ACKNOWLEDGEMENTS

GAH acknowledges support from the Dean's Doctoral Scholarship at the University of Manchester. CD/SEH/JPL/VS acknowledge funding from the STFC (Consolidated Grant ST/P000649/1) and CD/SEH from UKSA (LiteBIRD UK ST/Y005945/1). A.C. Taylor, M.E. Jones, and G. Weymann-Despres also acknowledge support from the Horizon Europe project RadioForegroundsPlus (GA 101135036), which is supported in the U.K. by UKRI grant number 10101603. This paper uses pre-publication data from the C-BASS project, which is a collaboration between Oxford and Manchester Universities in the U.K., the California Institute of Technology in the U.S., Rhodes University, UKZN and the South African Radio Astronomy Observatory in South Africa, and the King Abdulaziz City for Science and Technology (KACST) in Saudi Arabia. The work at Oxford was supported by funding from STFC, the Royal Society, and the University of Oxford. The work at the California Institute of Technology and Owens Valley Radio Observatory was supported by National Science Foundation (NSF) awards AST-0607857, AST-1010024, AST-1212217, and AST-1616227, and by NASA award NNX15AF06G. This work made use of standard scientific Python packages, including `NumPy` (Harris et al. 2020), `SciPy` (Virtanen et al. 2020), `Matplotlib` (Hunter 2007), `Astropy` (Astropy Collaboration 2013, 2018, 2022), `NaMaster` (Alonso et al. 2019), and `Healpy` (Zonca et al. 2019), which is based on the HEALPix framework (Górski et al. 2005).

DATA AVAILABILITY

The input data used in this work are publicly available from the respective survey archives. *Planck* HFI data were obtained from the *Planck* Legacy Archive (`https://pla.esac.esa.int/#home`). Cosmoglobe-processed WMAP and LFI data are available from the Cosmoglobe website (`https://www.cosmoglobe.uio.no/`). WMAP DR5 data were obtained from the NASA LAMBDA archive (`https://lambda.gsfc.nasa.gov/product/`). S-PASS data are available from the S-PASS collaboration website (`https://sites.google.com/inaf.it/spass`). QUIJOTE data were obtained from the QUIJOTE collaboration website (`https://research.iac.es/proyecto/quijote/pages/en/telescopes.php`). `Commander` is open-source software and available at `https://github.com/Cosmoglobe/Commander`. The C-BASS data used in this analysis are not yet publicly available but will be released in a future data release (Taylor et al. in prep.). The derived maps presented in this work will be made publicly available through the NASA LAMBDA archive upon publication.

REFERENCES

Ali-Haïmoud Y., Hirata C. M., Dickinson C., 2009, MNRAS, 395, 1055
Ali-Haïmoud Y., 2010, Astrophysics Source Code Library, pp 10016–
Alonso D., Sanchez J., Slosar A., LSST Dark Energy Science Collaboration 2019, MNRAS, 484, 4127
Andersen K. J., et al., 2023, A&A, 675, A13
Astropy Collaboration 2013, Astronomy & Astrophysics, 558, A33
Astropy Collaboration 2018, Astronomy & Astrophysics, 156, 123
Astropy Collaboration 2022, The Astrophysical Journal, 935, 167
Basak S., Delabrouille J., 2012, MNRAS, 419, 1163
Basak S., Delabrouille J., 2013, MNRAS, 435, 18
Bennett C. L., et al., 2003, ApJS, 148, 1
Bennett C. L., et al., 2013, ApJS, 208, 20
Bonaldi A., Ricciardi S., Leach S., Stivoli F., Baccigalupi C., de Zotti G., 2007, MNRAS, 382, 1791
Borrill J., et al., 2025, The Astrophysical Journal, 991, 23
Brandenburg A., Lazarian A., 2013, Space Sci. Rev., 178, 163
Cardoso J., Martin M., Delabrouille J., Betoule M., Patanchon G., 2008, IEEE Journal of Selected Topics in Signal Processing, 2, 735
Carretti E., et al., 2019, MNRAS, 489, 2330
Cepeda-Arroita R., 2022, Phd thesis, The University of Manchester, `https://bit.ly/45HHFj8`
Cepeda-Arroita R., et al., 2025, arXiv e-prints, p. arXiv:2510.05067
Delabrouille J., Cardoso J. F., Patanchon G., 2003, MNRAS, 346, 1089
Delabrouille J., et al., 2013, A&A, 553, A96
Dickinson C., Davies R. D., Davis R. J., 2003, MNRAS, 341, 369
Dickinson C., et al., 2018, New Astron. Rev., 80, 1
Draine B. T., 2011, Physics of the Interstellar and Intergalactic Medium. Princeton University Press
Draine B. T., Hensley B., 2013, ApJ, 765, 159
Draine B. T., Lazarian A., 1999, ApJ, 512, 740
Eriksen H. K., et al., 2004, ApJS, 155, 227
Eriksen H. K., Jewell J. B., Dickinson C., Banday A. J., Górski K. M., Lawrence C. R., 2008, The Astrophysical Journal, 676, 10
Fernández-Cobos R., Vielva P., Barreiro R. B., Martínez-González E., 2012, MNRAS, 420, 2162
Fernández-Torreiro M., et al., 2023, MNRAS, 526, 1343
Finkbeiner D. P., 2003, ApJS, 146, 407
Finkbeiner D. P., Davis M., Schlegel D. J., 1999, ApJ, 524, 867
Fixsen D. J., 2009, ApJ, 707, 916
Fixsen D. J., et al., 2011, The Astrophysical Journal, 734, 5
Galloway M., et al., 2023, A&A, 675, A3
Giardino G., Banday A. J., Górski K. M., Bennett K., Jonas J. L., Tauber J., 2002, A&A, 387, 82
Gold B., et al., 2009, ApJS, 180, 265
Górski K. M., Hivon E., Banday A. J., Wandelt B. D., Hansen F. K., Reinecke M., Bartelmann M., 2005, ApJ, 622, 759
Green S., Mackey J., Kavanagh P., Haworth T. J., Moutzouri M., Gvaramadze V. V., 2022, A&A, 665, A35
Han J. L., 2017, ARA&A, 55, 111
Harper S. E., et al., 2022, MNRAS, 513, 5900
Harper S. E., et al., 2025, MNRAS, 536, 2914
Harris C. R., et al., 2020, Nature, 585, 357
Haslam C. G. T., Salter C. J., Stoffel H., Wilson W. E., 1982, A&AS, 47, 1
Hunter J. D., 2007, Computing in Science & Engineering, 9, 90
Irfan M. O., 2023, MNRAS, 520, 6070
Irfan M. O., Puglisi G., 2025, arXiv e-prints, p. arXiv:2512.08522
Jew L., et al., 2019, MNRAS, 490, 2958
Jones M. E., et al., 2018, MNRAS, 480, 3224
Kogut A., 2012, ApJ, 753, 110
Kogut A., et al., 2007, ApJ, 665, 355
Leach S. M., et al., 2008, A&A, 491, 597
Leahy J. P., Cepeda-Arroita R., Dickinson C., et al., 2024, MNRAS, in prep.
Nasirudin A., Bull P., 2025, MNRAS, 544, 2419
Notari A., Quartin M., 2015, J. Cosmology Astropart. Phys., 2015, 047
Peel M. W., Genova-Santos R., Dickinson C., Leahy J. P., López-Caraballo C., Fernández-Torreiro M., Rubiño-Martín J. A., Spencer L. D., 2022, Research Notes of the American Astronomical Society, 6, 252
Planck Collaboration I 2016, A&A, 594, A1
Planck Collaboration II 2020, A&A, 641, A2

Planck Collaboration IV 2020, A&A, 641, A4
Planck Collaboration IX 2016, A&A, 594, A9
Planck Collaboration Int. XV 2014, A&A, 565, A103
Planck Collaboration VII 2016, A&A, 594, A7
Planck Collaboration VIII 2016, A&A, 594, A8
Planck Collaboration X 2016, A&A, 594, A10
Planck Collaboration XI 2014, A&A, 571, A11
Planck Collaboration XII 2014, A&A, 571, A12
Planck Collaboration XIII 2014, A&A, 571, A13
Planck Collaboration XIV 2014, A&A, 571, A14
Planck Collaboration XXV 2016, A&A, 594, A25
Planck Collaboration XXX 2014, A&A, 571, A30
Planck Collaboration et al., 2016, A&A, 594, A25
Platania P., Burigana C., Maino D., Caserini E., Bersanelli M., Cappellini B., Mennella A., 2003, A&A, 410, 847
Reich P., Reich W., 1988, A&AS, 74, 7
Remazeilles M., Delabrouille J., Cardoso J.-F., 2011, MNRAS, 418, 467
Remazeilles M., Dickinson C., Banday A. J., Bigot-Sazy M.-A., Ghosh T., 2015, MNRAS, 451, 4311
Remazeilles M., Dickinson C., Eriksen H. K. K., Wehus I. K., 2016, MNRAS, 458, 2032
Rubiño-Martín J. A., et al., 2012, in Stepp L. M., Gilmozzi R., Hall H. J., eds, Society of Photo-Optical Instrumentation Engineers (SPIE) Conference Series Vol. 8444, Ground-based and Airborne Telescopes IV. p. 84442Y, doi:10.1117/12.926581
Rubiño Martín J. A., et al., 2020, in Zmuidzinas J., Gao J.-R., eds, Society of Photo-Optical Instrumentation Engineers (SPIE) Conference Series Vol. 11453, Millimeter, Submillimeter, and Far-Infrared Detectors and Instrumentation for Astronomy X. p. 114530T, doi:10.1117/12.2561309
Rubiño-Martín J., et al., 2023, Monthly Notices of the Royal Astronomical Society, 519, 3383
Seljebotn D. S., Bærland T., Eriksen H. K., Mardal K. A., Wehus I. K., 2019, A&A, 627, A98
Silsbee K., Ali-Haïmoud Y., Hirata C. M., 2011, MNRAS, 411, 2750
Stevenson M. A., 2014, The Astrophysical Journal, 781, 113
Strong A. W., Orlando E., Jaffe T. R., 2011, A&A, 534, A54
Sunyaev R. A., Zeldovich Y. B., 1970, Ap&SS, 7, 3
Takekawa S., Oka T., Tanaka K., Matsumura S., Miura K., Sakai D., 2014, ApJS, 214, 2
Thorne B., Dunkley J., Alonso D., Næss S., 2017, Monthly Notices of the Royal Astronomical Society, 469, 2821–2833
Virtanen P., et al., 2020, Nature Methods, 17, 261
Watts D. J., et al., 2023, A&A, 679, A143
Watts D. J., et al., 2024, A&A, 686, A297
Wilensky M. J., Irfan M. O., Bull P., 2025, MNRAS, 539, 3122
Zerafa D. P., Wilkinson P. N., Radcliffe C. J., Leahy J. P., Browne I. W. A., Black P. J., 2025, RAS Techniques and Instruments, 4, rzaf017
Zonca A., Singer L. P., Lenz D., Reinecke M., Rosset C., Hivon E., Gorski K. M., 2019, Journal of Open Source Software, 4, 1298
Zonca A., Thorne B., Krachmalnicoff N., Borrill J., 2021, Journal of Open Source Software, 6, 3783
de Oliveira-Costa A., Tegmark M., Gaensler B. M., Jonas J., Landecker T. L., Reich P., 2008, MNRAS, 388, 247
de la Hoz E., et al., 2023, MNRAS, 519, 3504

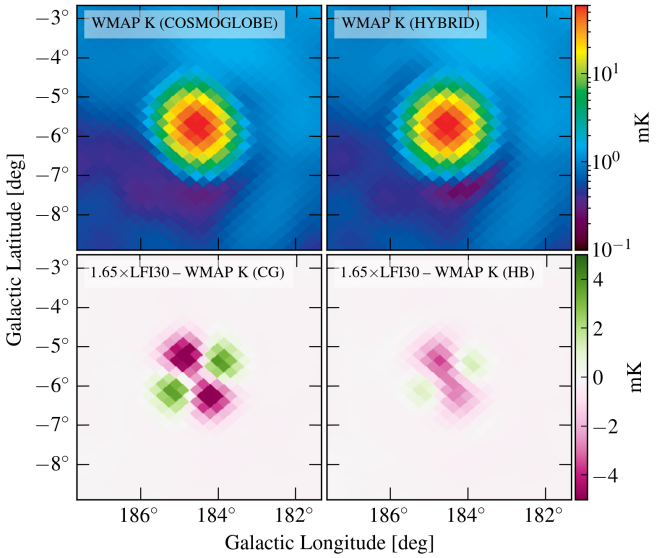

Figure A1. Effect of the hybrid map construction in the WMAP K-band. Top panels: Cosmoglobe map (left) and hybrid map (right). Bottom panels: residuals relative to the scaled *Planck* LFI 30 GHz map, highlighting the reduction of quadrupolar artefacts around bright sources in the hybrid version.

APPENDIX A: HYBRID WMAP MAP CONSTRUCTION

The Cosmoglobe WMAP maps were not beam-symmetrised during map-making, and point sources therefore retain the elliptical shape of the native instrumental beams, most prominently in the K- and Ka-bands. In component separation runs in the pixel space, these elliptical beam patterns produce quadrupolar residuals around bright compact sources due to mismatches in source morphology across frequency channels.

To mitigate this effect, we construct hybrid K- and Ka-band maps that combine the large-scale structure of the Cosmoglobe maps with the small-scale information of the original symmetrised WMAP DR5 maps. The combination is performed in harmonic space using two complementary window functions,

$$B_\ell^{\rm L} = \cos^2\left(\frac{\pi}{2}\cdot\frac{\ell-\ell_0}{\ell_{\rm f}-\ell_0}\right), \quad B_\ell^{\rm S} = \cos^2\left(\frac{\pi}{2}\cdot\frac{\ell-\ell_{\rm f}}{\ell_{\rm f}-\ell_0}\right), \tag{A1}$$

where ℓ_0 and $\ell_{\rm f}$ define the transition region in multipole space. The hybrid map is then

$$a_{\ell m}^{\rm hybrid} = B_\ell^{\rm L}\, a_{\ell m}^{\rm Cosmoglobe} + B_\ell^{\rm S}\, a_{\ell m}^{\rm WMAP}. \tag{A2}$$

We adopt $\ell_0 = 32$ and $\ell_{\rm f} = 64$, which correspond to angular scales around the beam size after smoothing to 1° resolution. This choice preserves the improved large-scale calibration of Cosmoglobe while restoring circularised small-scale source morphology from the original WMAP maps. The procedure is applied only to the K- and Ka-bands since in the higher-frequency channels, beam asymmetries are sufficiently small that no correction is required. Figure A1 illustrates the impact of this correction in the K-band, showing the reduction of quadrupolar artefacts around bright compact sources.

APPENDIX B: MONOPOLE, DIPOLE AND INSTRUMENTAL PARAMETERS POSTERIORS

This appendix summarises the procedures used to determine the monopole and dipole offsets of the low-frequency surveys employed in this work. The resulting monopole, dipole, calibration, and bandpass-shift parameters are listed in Table B1, and the method used to estimate the monopole of each low-frequency channel is described below.

C-BASS — The C-BASS monopole was recalibrated through a T–T analysis against the *Planck* 2015 model prediction at 4.76 GHz. The comparison was performed at $N_{\rm SIDE}$ 64 using the PM61 mask. The fitted intercept was 21 ± 1 mK, approximately half of the correction implied by the ARCADE 2-based calibration. Internal runs showed that adopting this value produced stable solutions and physically plausible synchrotron spectral indices. No statistically significant dipole correction was required for C-BASS.

S-PASS — A direct T–T calibration of S-PASS against the *Planck* 2015 model was found to be unreliable due to large-scale structural differences in the southern sky. Instead, morphological continuity between S-PASS and C-BASS was enforced in their overlap region. Holding the C-BASS solution fixed, five large-scale correction parameters were fitted to S-PASS: a global amplitude/spectral index scaling, a monopole term, and three dipole components. The minimisation yielded an effective spectral index of $\beta = -3.12$ and removed visible discontinuities between the surveys. The resulting monopole and dipole values were adopted as the S-PASS offsets.

QUIJOTE — QUIJOTE monopoles were estimated through T–T correlations between preliminary runs excluding QUIJOTE and the QUIJOTE maps within the adopted Galactic-plane mask. Compact sources were masked using the PS30 mask. This procedure was applied to the 11, 13, 17, and 19 GHz channels. The offsets for all the QUIJOTE channels were consistent within 1σ with the Rubiño-Martín et al. (2023). No statistically significant dipole correction was required within the plane region used.

Cosmoglobe WMAP and LFI — Cosmoglobe-reprocessed WMAP and LFI maps exhibit offset shifts of order ∼ 10 µK relative to their original releases. For these channels, the *Planck* 2015 monopole and dipole normalisation scheme is retained, and residual offsets are adjusted through T–T correlations at $N_{\rm SIDE} = 64$ using the PM61 mask.

APPENDIX C: DERIVED SPECTRAL INDEX MAPS

Although our baseline analysis directly samples the synchrotron spectral index $\beta_{\rm s}$ within the parametric component-separation, effective spectral index maps can also be constructed in the traditional manner from the modelled sky emission. This allows direct comparison with literature spectral index products defined between specific frequency pairs.

For two frequencies ν_1 and ν_2, the effective spectral index $\beta(\nu_1, \nu_2)$ is computed pixel by pixel assuming a local power-law behaviour of the brightness temperature,

$$T(\nu) \propto \nu^\beta, \tag{C1}$$

which leads to

$$\beta(\nu_1, \nu_2) = \frac{\log[T(\nu_1)/T(\nu_2)]}{\log(\nu_1/\nu_2)}. \tag{C2}$$

In our case, the brightness temperatures $T(\nu_1)$ and $T(\nu_2)$ are obtained from the full sky model evaluated at the corresponding frequencies, including all components. These maps therefore represent the effective spectral behaviour of the total emission or of a specific component,

Table B1. Monopoles, dipoles, calibration factors and bandpass corrections derived within the baseline temperature model.

Survey	Frequency [GHz]	Detector label	Monopole [μK]	*X* dipole [μK]	*Y* dipole [μK]	*Z* dipole [μK]	Calibration [%]	Bandpass shift [GHz]
S-PASS	2.30	...	146 [a,b]	36 [a,b]	62 [a,b]	65 [a,b]	0 [a]	0 [a]
C-BASS	4.76	...	21 [a,b]	0 [a]	0 [a]	0 [a]	0 [a]	0 [a]
QUIJOTE	11.1	...	−826 [a]	0 [a]	0 [a]	0 [a]	0 [a]	0 [a]
	12.9	...	−490 [a]	0 [a]	0 [a]	0 [a]	0 [a]	0 [a]
	16.8	...	−529 [a]	0 [a]	0 [a]	0 [a]	0 [a]	0 [a]
	18.8	...	−942 [a]	0 [a]	0 [a]	0 [a]	0 [a]	0 [a]
WMAP	22.8	K	−31 ± 1	−6.5 ± 0.2	5.1 ± 0.1	−6.8 ± 0.1	0 [a]	0 [a]
	33.0	Ka	−15 [a]	−3.8 ± 0.1	4.6 ± 0.1	−7.9 ± 0.1	−0.0 ± 0.1	0 [a]
	40.6	Q1	−10 ± 1	−3.0 ± 0.1	3.5 ± 0.1	−6.3 ± 0.1	−0.1 ± 0.1	0 [a]
		Q2	−9 ± 1	−3.1 ± 0.1	3.7 ± 0.1	−6.4 ± 0.1	0.1 ± 0.1	0.2 ± 0.1
	60.8	V1	−3 ± 1	−2.7 ± 0.1	1.2 ± 0.1	−3.7 ± 0.1	0.1 ± 0.1	0 [a]
		V2	−3 ± 1	−2.7 ± 0.1	1.2 ± 0.1	−3.6 ± 0.1	0.4 ± 0.1	−0.2 ± 0.1
	93.5	W1	−15 ± 1	−1.8 ± 0.1	−0.6 ± 0.1	−2.9 ± 0.1	0.4 ± 0.1	0 [a]
		W2	−13 ± 1	−2.1 ± 0.1	−0.5± 0.1	−2.7 ± 0.1	0.6 ± 0.1	−0.2 ± 0.4
		W3	−17 ± 1	−1.8 ± 0.1	−1.0 ± 0.1	−3.0 ± 0.1	−0.0 ± 0.1	0.9 ± 0.5
		W4	−14 ± 1	−1.9 ± 0.1	−0.5 ± 0.1	−2.6 ± 0.1	0.4 ± 0.1	−0.1 ± 0.4
Planck LFI	28.4	all	−20 ± 1	−6 [a]	3 [a]	−6 [a]	0.6 ± 0.1	0.3 ± 0.1
	44.1	all	−8 ± 1	−4.4 ± 0.1	0.5 ± 0.1	−3.4 ± 0.1	0.2 ± 0.1	0.0 ± 0.1
	70.3	all	−3 ± 1	−3.8 ± 0.1	−1.9 ± 0.1	−0.6 ± 0.1	0.8 ± 0.1	0.0 ± 0.1
Planck HFI	100	ds1	9 [a]	0 [a]	0 [a]	0 [a]	0.11 ± 0.01	0.4 ± 0.6
		ds2	7 ± 1	0.1 ± 0.1	0.0 ± 0.1	0.1 ± 0.1	0.07 ± 0.01	0.6 ± 0.6
	143	ds1	21 [a]	0 [a]	0 [a]	0 [a]	0 [a]	0.9 ± 0.1
		ds2	22 ± 1	0.1 ± 0.1	0.0 ± 0.1	−0.1 ± 0.1	−0.04 ± 0.01	0.0 ± 0.1
		5	21 ± 1	−0.5 ± 0.1	0.0 ± 0.1	−0.2 ± 0.1	0.09 ± 0.01	−0.2 ± 0.1
		6	21 ± 1	−0.4 ± 0.1	0.0 ± 0.1	−0.2 ± 0.1	0.12 ± 0.01	0.5 ± 0.1
		7	21 ± 1	−0.2 ± 0.1	0.0 ± 0.1	−0.1 ± 0.1	0.01 ± 0.01	−0.1 ± 0.1
	217	1	63 ± 1	−1.3 ± 0.1	−3.5 ± 0.1	3.9 ± 0.1	0 [a]	−0.2 ± 0.1
		2	63 ± 1	−1.2 ± 0.1	−3.5 ± 0.1	4.0 ± 0.1	0.01 ± 0.01	−0.3 ± 0.1
		3	61 ± 1	−1.5 ± 0.1	−3.7 ± 0.1	4.1 ± 0.1	−0.03 ± 0.01	−0.1 ± 0.1
		4	63 ± 1	−1.0 ± 0.1	−3.7 ± 0.1	4.1 ± 0.1	0.02 ± 0.01	−0.3 ± 0.1
	353	ds2	428 ± 2	−4 ± 1	−7 ± 1	7 ± 1	−0.0 ± 0.1	0.2 ± 0.1
		1	427 ± 3	−5 ± 1	−17 ± 1	17 ± 1	0.3 ± 0.1	0.0 ± 0.1
	545	2	0.37 [a,c]	0 [a]	0 [a]	0 [a]	−2.8 [a]	2.0 [a]
		4	0.36 ± 0.01 [c]	0 [a]	0 [a]	0 [a]	−3.2 [a]	2.8 [a]
	857	2	0.64 ± 0.01 [c]	0 [a]	0 [a]	0 [a]	1.7 [a]	5.8 [a]

Notes: [(a)] Fixed at reference value. [(b)] Unit is mK. [(c)] Unit is MJy/sr.

depending on the model outputs used. Figure C1 shows examples of spectral index maps derived from our solution using different frequency pairs. These maps illustrate how the effective spectral index captures the frequency-dependent behaviour of Galactic foreground emission. Spectral indices defined between different frequency pairs probe distinct spectral regimes, resulting in systematic differences in the inferred slopes. This frequency-range dependence must be taken into account when comparing spectral index maps derived from different data combinations.

This paper has been typeset from a TEX/LATEX file prepared by the author.

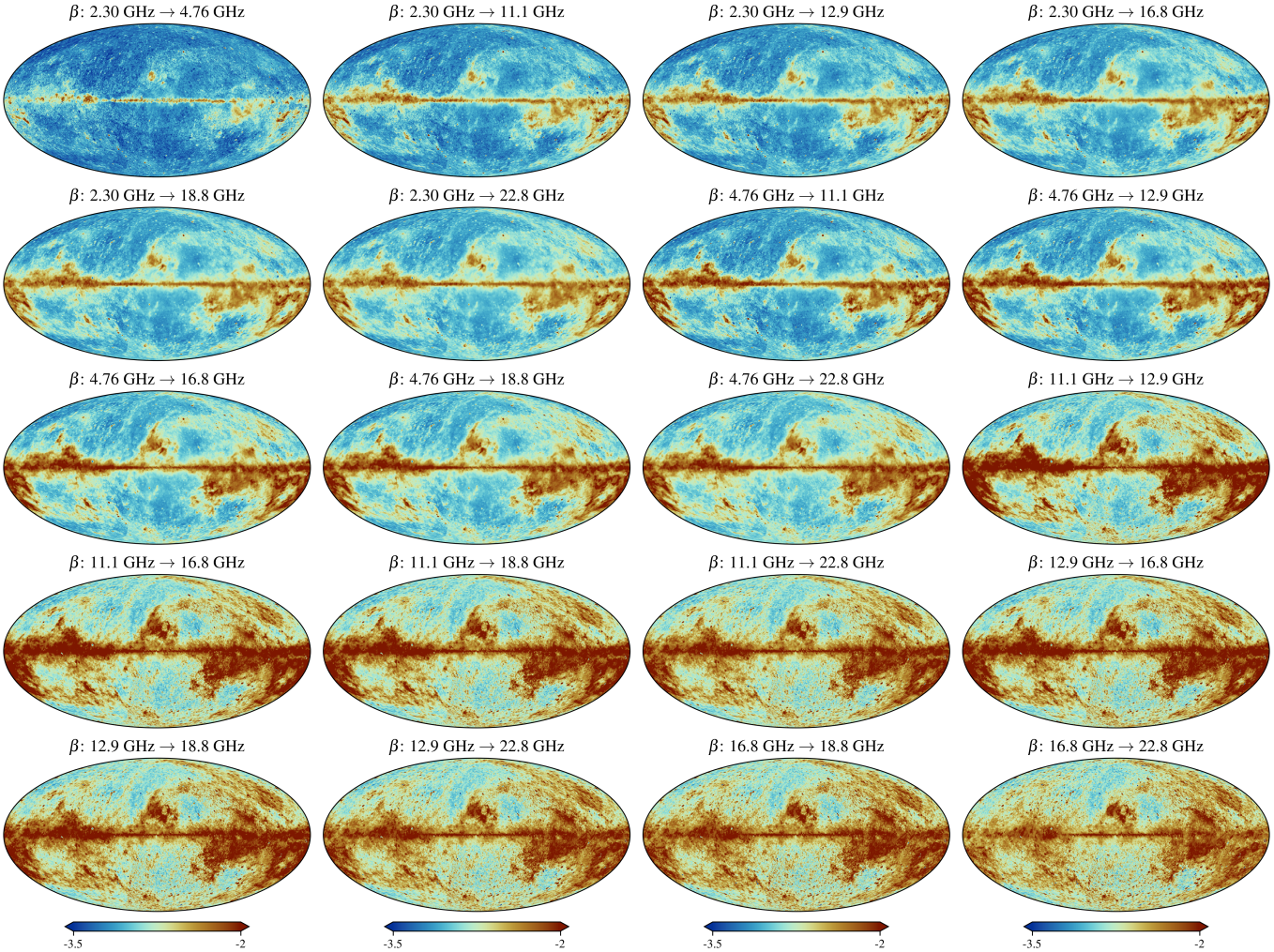

Figure C1. Examples of effective spectral index maps derived from the sky model presented in this work using different frequency pairs. The indices are computed pixel by pixel assuming a local power-law behaviour of the brightness temperature (Eq. C2).